Meson symmetries from Screening Masses in N_f=2 lattice QCD at High Temperatures

---

David Ward

A Dissertation from the

Department of Physics – International Physics Course

The University of Osaka

Version of July 28, 2025

Abstract

Quantumchromodynamics ("QCD") as a theory which describes the strong nuclear force is a robust theory which has been able to describe myriad phenomena. However, study of QCD is made difficult for perturbative approaches at finite temperatures by the non-abelian nature of the gauge fields. Therefore, non-perturbative approaches to QCD such as those offered by the framework of lattice quantum field theory has proven successful in studying such finite temperature phenomena. Chiral symmetry, broken spontaneously at low temperatures, is a phenomena which is essential to understanding the scale of hadronic mass in the universe as well as properties of deconfined quark and gluon matter at very high temperatures. The chiral crossover, the point of restoration for chiral symmetry, occurs at high but finite temperatures and is ideal to be studied from the lattice.

To this end we simulate two flavor lattice QCD using Möbius Domain wall fermions to investigate the symmetries of mesons associated with the spatial two-point correlation function at high temperatures. The temperatures we consider in this investigation range from $T = 147$MeV to $T = 330$MeV which cover the critical temperature $T_c = 165$MeV. Our choice of the Möbius Domain wall fermions offers us an excellent chiral symmetry on the lattice with an approximate violation of the Ginsparg-Wilson relation of 0.14MeV for a lattice cut off of $a^- = 2.643$GeV corresponding to a fine lattice.

From the two-point correlation function we extract the long range screening mass for incremental values in the temperature; and using the difference in the screening masses as a probe we investigate $SU(2)_L \times SU(2)_R$ chiral symmetry, the axial $U(1)_A$ which is broken by quantum anomaly, and additional emergent high temperature symmetry which exchanges spin degrees of freedom. In addition to the screening mass difference we also explore the temperature dependence of the screening mass itself and evaluate how the screening mass approaches both the $T = 0$ meson spectrum, as well as, the leading order of the perturbative predicition of twice the groundstate Matsubara mass $2\pi T$.

Contents

Chapter 1

Introduction

Quantum Chromodynamics(QCD) is a tremendously successful theory describing the multitude of hadronic and mesonic phenomena which we have observed in the 20th century alone. While the theory can be neatly written down in three terms, the analytical approaches to the theory have encountered considerable difficulty owing to the non-abelian nature of the gauge fields described by the $SU(3)$ gauge theory, in addition to subtleties of the stronger interactions which can be explored in effective theories. While this has meant difficulty for the approach to pertubrative expansion of the propagator in QCD via Feynman diagram style calculations, it has led to a very rich theoretical description by way of lattice calculations.

The lattice formalism which is now half a century old, has made great progress in both analytical and numerical studies of strongly coupled theories like QCD; while there is still much we do not fully understand in QCD we have been able to understand more of the subtle phenomena in low temperature hadronic physics. As the perturbative apporach to QCD is only accessible at extreme temperatures for finite but high temperatures, the lattice offers an attractive set of tools to study the properties of mesons and hadrons non-pertubratively.

The range of temperatures for which the lattice can be connected back to the perturbative phenomena and thus the range of temperatures at which the coupling becomes "weak" is not clear even still. There are several effective theories such as non-relativistic quantum field theory and its extension to QCD, non-relativistc quantumchromodynamics, which can be applied at finite but very high temperatures. In the case of the latter, several predictions from this perturbative framework have been made but the scale at which the physics is relevant is still unclear despite studies done by several collaborations on the subject [1, 2]. We will explore this subject and discuss the the thermal behaviors of the meson at high temperatures in later chapters.

Another essential question in QCD is that of chiral symmetry. Chiral symmetry is an essential phenomena in hadron formation as it gives rise to the pion mass and the scale of hadronic masses $\sim \mathcal{O}(1\text{GeV})$ when spontaneously broken. As this is a phenomena which is known to be broken at low temperatures, it is understood that at high temperatures there is a present chiral symmetry which must have broken spontaneously in the history of the early universe. As chiral symmetry is exact in the case of massless quarks the breaking of this symmetry does not result in a massless goldstone boson but a massive psuedo-goldstone boson, the pion.

Due to this we expect that the lightest two quark flavors, the up and down quark,

which are roughly degenerate, play a critical role in the phase transition. As it happens the details of the critical phenomena depend on the symmetry of these quarks above the critical temperature T_c [3].

The order parameter for the breaking of chiral symmetry, the chiral condensate, indicates that in the massless limit of the up and down quarks the critical temperature is on the order of $150 - 200$MeV. At these temperatures the vector like chiral symmetries $SU(2)_L \times SU(2)_R$ are fully resotred and the chiral condensate vanishes.

Naively we expect that this is the extent of the restoration for chiral symmetry as there are no additional broken symmetries. However, the $U(1)_A$ broken by quantum anomaly which has been shown to have a relationship the chiral condensate [4, 5, 6, 7], may appear if the topological exciations resulting from gluonic fluctuations become suppressed above T_c. The roots for this will be discussed in the next chapter.

There is an ongoing interest in the exact point of restoration for $U(1)_A$ as this impacts the universality of the phase transition. To this end, there is a large body of work which has looked at the topological fluctuations as effectively described by instantons [8, 9, 10, 11], in the cases of pure Yang-Mills, large N_c color degrees of freedom and QCD with heavy quarks. In the context of these studies the instantonic effects persist at temperatures $T \sim T_c$ and thus continue to drive susceptibility to the quantum anomaly keeping $U(1)_A$ broken. However, in the case of $N_c = 3$ with light dynamical quarks, the size of these gluonic effects are on the order of pion physics and thus subject to a larger correlation length, in such a setting the topological fluctuations are not longer described by the instanton gas.

At very high temperatures the work done in [12] using the NRQCD$_3$ approach predicted a spin independent correction to the spatial screening mass of all meson states, in addition to the leading order $2\pi T$ term. This seems to imply that all the meson states become degenerate in the high temperature limit and may become more symmetric. This leading order term which is well known as twice the groundstate of the Matsubara mass.

In addition to this there is a recent body of work which asserts the presence of emergent symmetry structure at $T \sim 2T_c$ and above [13, 14, 15, 16, 17, 18, 19]. This approximate symmetry called chiral-spin symmetry may actually be related to this perturbative prediction as the high temperature mesons develop a spin independent symmetry which is analogous to the heavy quark symmetry at $T = 0$ [20, 21]. This symmetry which emerges due to a large Matsubara mass is only an approximate symmetry which may be enhanced by gluonic effects making it emergent at temperatures around $2T_c$.

It is important to stress, in contrast to the chiral symmetry mentioned previously, this chiral-spin symmetry and other possibly emergent larger symmetry structure in high temperature QCD is not a symmetry which is present in the original QCD Lagrangian but a symmetry which may be seen from the free quark propagator in the large T limit.

In addition to looking at the analytical roots for these symmetries in QCD we will present the results of lattice simulations of QCD using the Möbius Domain Wall fermions at high temperatures to investigate the symmetries of the mesons. Previously this work has been done by other collaborations using different lattice fermion operators, however, these fermion formulations expliciltly broke the $SU(2)_L \times SU(2)_R$ chiral symmetry. Previous work done with Wilson fermions worked with a remnant vector like $SU(2)_V$ symmetry; while work done with the staggered fermions broke the chiral symmetry to $U(1)'_V \times U(1)'_A$, a distinct remnant symmetry from the quark number and anomalous $U(1)$ symmetries present in the

original QCD Lagrangian. Work done by JLQCD [22, 23, 24] showed that lattice artifact are enhanced in the probes for $U(1)_A$ at high temperatures, making it difficult to distinguish genuine breaking from discretization artifacts. This makes study of chiral symmetry using a theoretically clean approach like the Möbius Domain Wall fermions attractive as we can simplify our analysis procedures and avoid any additional artifacts which may be introduced in the Wilson fermion and Staggered fermion formulations.

Due to the critical interest we have in both $SU(2)_L \times SU(2)_R$ and $U(1)_A$ chiral symmetries it is our interest to study both symmetries at high temperatures near the critical point by lattice simulation using Möbius Domain wall fermions. Due to the exact form of chiral symmetry maintained by the Möbius domain wall fermions we can achieve a more straightfoward analysis thereby allowing us to better extract the physics of the chiral crossover.

Our particular interest in this region is characterizing the behaviors of the mesonic two point correlation functions using the spatial screening mass differences as a probe of the chiral symmetry. To this end we examine a series of latices associated with a range of temperatures from $T = 174 - 330$MeV or $[0.9 - 2.0]T_c$ where the T_c is estimated from the peak of chiral susceptibility [6].

In this work, we will study the restoration of chiral symmetry surrounding the critical temperature T_c, specifically we will focus on probes for $SU(2)_L \times SU(2)_R$ and $U(1)_A$ drawn from the long range screening mass of the flavor isospin triplet two-point meson correlation function. We are interested in both the temperature of restoration for the chiral symmetries as well as their symmetry behaviors above T_c, in particular, how the meson masses approach the perturbative leading order predicition of $2\pi T$. Due to the preservation of a theoretically clean chiral symmetry from the Möbius domain wall fermions, we expect that our probe for chiral symmetries to be reliable through the range of temperatures in our study.

In addition to study of chiral symmetries at high temperatures, we will also investigate the possibility of an emergent approximate isospin $SU(2)$ symmetry due to the large thermal mass in the range $T_c - 2T_c$. Following the evidence presented in previous studies [15, 25, 26], as well as, theoretical arguments which we will explore in detail later, there we expect to find a threshold for which this symmetry becomes accessible at high temperatures.

In consideration of the points laid out above the organization of this thesis is as follows. In Chapter 2 we will briefly revisit the core symmetries of the Lagrangian and explore the relationship between the breaking of chiral symmetry and the chiral condensate, as well as discuss briefly the relationship between the topological chrgae fluctuation and the axial anomaly.

Following this we will then connect chiral symmetry to the lattice in Chapter 3 and discuss how lattice discretization leads to doublers, how to eliminate these doubler effects while also preserving a theoretically exact form of the chiral symmetry on the lattice.

In Chapter 4 we will discuss the finite temperature lattice, mesonic two point functions and their high temperature thermal behaviors leading to the perturbative results from [12].

We will then cover the high temperature behaviors of the meson correlation functions, the probes for symmetries from the spatial correlation functions and the emergent high temperature symmetry $SU(2)$ chiral-spin($SU(2)_{CS}$) in Chapter 5.

Finally we will present the results of the lattice simulations and highlight both the thermal properties of the mesons as well as the change in symmetries with respect to temperature, and an evaluation of errors in our calculation in Chapter 6.

Chapter summarizes the previous chapters and discusses the lattice results in relationship to the broader body of work in QCD.

The core of this work is already published under [27] and part of this was previously presented at Lattice 2024 [28], in addition to this, related work on $N_f = 2 + 1$ QCD which influenced this work was presented at Lattice 2023 [29]. See [5, 30, 31, 32, 33] for additional work done by JLQCD on the chiral symmetry in finite temperature QCD.

Chapter 2

Symmetries of Quantum Chromodynamics

In order to discuss nonperturbative studies of quarks and their fundamental symmetries at finite temperature we need to begin with the most low to the ground part of the description of the interactions of fermions in quantum chromodynamics(QCD) and explore the necessity of the lattice.

As the more complicated and subtle pieces of QCD stem from the fact that the entire theory is not easily described perturbatively we can write out the theory quite neatly to frame our broader discussion.

2.1 QCD in a nutshell

The Lagrangian for QCD is quite simple and is written in three terms:

$$\mathcal{L} = i\bar{\psi}(x)\not{D}\psi(x) + m\bar{\psi}(x)\psi(x) + \frac{1}{2g^2}\mathrm{tr}[F_{\mu\nu}F^{\mu\nu}]. \tag{2.1}$$

While the Lagrangian describing QCD is quite compact, the complexities of QCD run quite deep and are not obvious from the form of the Lagragian on its own. The complexity is actually connected to the many symmetries of the Lagrangian. One symmetry of the Lagrangian that is the most difficult is actually the gauge symmetry of the "color" field. The complexity of non-abelian fields lies in their ability for self interaction and in the case of QCD the strength of their interactions.

2.1.1 Non-Abelian Gauge Theories and the fermion propagator

While there are some very important properties of the $U(1)$ gauge theory which are relevant to the fundamental symmetries of quarks in QCD, we will revisit these after a quick primer in a leading reason for study of quark field theories on the lattice: the non-abelian gauge field. As $U(1)$ is a group constructed from straightforward continuous transformations, the group elements simply commute. However, this can be generalized to incorporate non-trivial

gauge transformations composed of generators for any group $SU(N)$. The extension of the gauge transformation is

$$A_\mu \to A^a_\mu(x)T^a + \partial_\mu \theta^a(x)T^a - igA^a_\mu(x)\theta^b(x)[T^a, T^b], \tag{2.2}$$

wherein T^a is a generator for the Lie group $SU(N)$.The procedure for writing the gauge transformations are easily written down:

$$G(x) = e^{-ig\theta^a(x)T^a}. \tag{2.3}$$

The generators obey the following commutation relation

$$[T^a, T^b] = if^{abc}T^c, \tag{2.4}$$

which exposes the structure constant f^{abc}. As the generators no longer straightforwardly commute the gauge transformations now obey the rules of a group and so can no longer easily commute through terms in the Lagrangian. This has the consequence of making field interactions much more complicated and allowing for self interactions between gauge fields.

The most obvious case for this is seen in the redescription of the field strength tensor which now contains the commutator of the vector potential,

$$\begin{aligned} F_{\mu\nu} &= \partial_\mu A_\nu - \partial_\nu A_\mu - ig[A_\mu, A_\nu], & (2.5)\\ &= (\partial_\nu A^c_\mu - \partial_\mu A^c_\nu + gf^{abc}A^a_\mu A^b_\nu)T^c. & (2.6) \end{aligned}$$

Due to the noncommutation of the generators again we can see that the field tensor now gains an extra self-interaction term and an explicit field index. Due to the additional index in the path action the gauge field action must now have an explicit trace over the index,

$$\mathcal{L} = i\bar{\psi}(x)\not{\mathcal{D}}\psi(x) + m\bar{\psi}(x)\psi(x) + \frac{1}{2g^2}\mathrm{tr}[F_{\mu\nu}F^{\mu\nu}]. \tag{2.7}$$

While this form of the Lagrangian looks very much similar to the form of the $U(1)$ gauge theory with fermions, there is a critical difference: the $SU(N)$ gauge fields and their self interactions lead to a much more complicated beta function. The form of which looks like

$$\beta(g) = -\left[\frac{11}{3}N - \frac{2}{3}N_f\right]\frac{g^3}{16\pi^2} + \mathcal{O}(g^5), \tag{2.8}$$

for QCD where $N = 3$ the coupling remains negative for any theory of fermions with less than $N_f = 16$. This means that the low energy gauge coupling of QCD is incredibly strong and weakens at high energies. In this case low energy perturbation theory which we can perform for the $U(1)$ theory breaks down and so cannot be used to investigate the behaviors quarks and gauge fields. To proceed actually studying the low energy region of QCD < 1GeV we require an alternative approach to the path integral not using perturbative techniques, we therefore require a lattice formulation of QCD.

2.2 Fermion Propagator and Chiral Symmetry

Independent of the gauge field symmetry of interacting fermions there is an additional global set of symmetries inherent to the fermions which we will also now explore. The chiral and flavor symmetries of the fermions are of importance to the study of QCD and specifically the chiral symmetry is critically impacted by the reformulation of the continuum theory for the lattice. To build our way to the lattice let us consider the most simplistic theory of fermions which are noninteracting.

$$\mathcal{L} = i\bar{\psi}\partial\!\!\!/\ \psi + m\bar{\psi}\psi \tag{2.9}$$

Our goal overall is to understand chrial symmetry in the context of QCD, in the non-interacting fermion Lagrangian we can already see the present chiral symmetry. Introducing projectors

$$P_L = \frac{1-\gamma_5}{2} \qquad P_R = \frac{1+\gamma_5}{2} \tag{2.10}$$

Which have a range of properties inherited from the anticommutator for the gamma matrices

$$\{\gamma_\mu, \gamma_\nu\} = 2\delta_{\mu\nu}. \tag{2.11}$$

Specifically the fact that

$$\gamma_5 = i\gamma_0\gamma_1\gamma_2\gamma_3, \tag{2.12}$$

where γ_5 anticommutes with all other gamma matrices. Based on this property and some basic identities derived from the forms of the projectors we can introduce these into the Lagrangian:

$$\mathcal{L} = \bar{\psi}(x)(P_L+P_R)i\gamma_\mu\partial_\mu(P_L+P_R)\psi(x) + m\bar{\psi}(x)(P_L+P_R)\psi(x)(P_L+P_R). \tag{2.13}$$

Using the anticommuting property of the gamma matrices we can establish

$$P_L\gamma_\mu = \gamma_\mu P_R, \tag{2.14}$$

combined with the property that

$$P_R P_L = 0, \tag{2.15}$$

the Lagrangian becomes

$$\mathcal{L} = i\bar{\psi}(x)P_L\partial\!\!\!/\ P_R\psi(x) + i\bar{\psi}(x)P_R\partial\!\!\!/\ P_L\psi(x) + m\bar{\psi}(x)(P_L^2+P_R^2)\psi(x). \tag{2.16}$$

When the projectors are applied to the fermions they sectorize into right propagating and left propagating:

$$\psi_R(x) = P_R\psi(x) \qquad \bar{\psi}_R(x) = \bar{\psi}(x)P_L, \tag{2.17}$$

$$\psi_L(x) = P_L\psi(x) \qquad \bar{\psi}_L(x) = \bar{\psi}(x)P_R. \tag{2.18}$$

Thus the kinetic term in the Lagrangian separates into two independent chiral sectors, while the mass term mixes the left and right chiral fermions.

$$\mathcal{L} = i\bar{\psi}_R\partial\!\!\!/\ \psi_R + i\bar{\psi}_L\partial\!\!\!/\ \psi_L + m(\bar{\psi}_R\psi_L + \bar{\psi}_L\psi_R) \tag{2.19}$$

For the noninteracting fermion theory as in all the theories with fermions to follow the chiral symmetry is exact in the massless limit; this limit known as the chiral limit can be approximated in fermionic theories with multiple flavors as an approximate symmetry for light fermions. To understand this better we will explore the continuous chiral transformation applied to the unflavored fermions first.

The Lagrangian in the chiral limit is actually invariant under chiral transformation of the fermions in the following way

$$\psi(x) \rightarrow e^{i\alpha\gamma_5}\psi(x) \tag{2.20}$$
$$\bar{\psi}(x) \rightarrow \bar{\psi}(x)e^{i\alpha\gamma_5} \tag{2.21}$$

When all fermions in the Lagrangian are transformed the kinetic term is again invariant while the mass term mixes the chiral transformation,

$$\mathcal{L} = i\bar{\psi}(x)\partial\!\!\!/\,\psi(x) + m\bar{\psi}e^{2i\alpha\gamma_5}\psi. \tag{2.22}$$

Complicating this further we can introduce flavor into the mix of chiral symmetry as well. The flavor symmetry is a global symmetry between the different flavor states that a fermion can occupy. In the case of quarks there are six known flavors, however, depending on the energetic regime of the theory of interest this flavor structure can take on different symmetry group representations.

2.2.1 Flavor and Chiral Symmetry

In the case of the flavored theory of fermions the spinor ψ is now a N_f entry vector while the mass parameter m becomes an $N_f \times N_f$ diagonal matrix with entries corresponding to the mass of each flavor. In the theory with N_f degenerate flavors the mass matrix is simply m multiplied onto identity.

Flavor is a global transformation of the entire fermion action which has the following structure:

$$\mathrm{Tr}[F^a, F^b] = \frac{1}{2}\delta_{ab}, \tag{2.23}$$

$$F^a \in \{F^s, F^n\}, \quad F^s \equiv \mathbb{1}_{N_f \times N_f}, \quad F^n \in \{\text{Generators of } SU(N_f)\}, \quad n = 1, \ldots, N_f^2 - 1. \tag{2.24}$$

The matrices F^n are the generators of the $SU(N_f)$ symmetry group where the group structure is dependent on the number of flavors of the theory. The group is split between the singlet transformation F^s and the non-singlet flavor mixing transformations in the rest of the group, which we have written as F^n.

Under this symmetry group the fermions transform with an additional $N_f \times N_f$ vector symmetry which are divided into the flavor mixing and singlet transformations

$$\psi \rightarrow e^{i\theta_n F^n}\psi, \qquad \bar{\psi} \rightarrow \bar{\psi}e^{-i\theta_n F^n}, \tag{2.25}$$
$$\psi \rightarrow e^{i\theta\mathbb{1}}\psi, \qquad \bar{\psi} \rightarrow \bar{\psi}e^{-i\theta\mathbb{1}}. \tag{2.26}$$

One method of treating the simultaneous chrial and flavor transformations is to break these into the set of vector and axial vector transformations:

$$\psi \to e^{i\theta_n \gamma_5 F^n}\psi, \qquad \bar{\psi} \to \bar{\psi} e^{i\theta_n \gamma_5 F^n} \qquad SU(N_f)_A, \tag{2.27}$$

$$\psi \to e^{i\theta_n F^n}\psi, \qquad \bar{\psi} \to \bar{\psi} e^{-i\theta_n F^n} \qquad SU(N_f)_V, \tag{2.28}$$

as well as the corresponding singlet flavor transformations. However, these transformations are not directly consistent with the projectors we previously considered; when applied simultaneously with the corresponding left and right handed projections the flavor transformations applied to the fermions sectorize into a left and right handed $SU(N_f)$ symmetry:

$$SU(N_f)_L \times SU(N_f)_R \times U(1)_V \tag{2.29}$$

Although the previous flavor transformations were not constructed as chiral explicitly the chiral symmetry of the overall theory is incorporated as a direct product with the flavor mixing angle as the chiral transformation applies to each flavor individually. The previously mentioned axial transformation, can also be applied as a separate transformation to the Dirac spinors indicating that the total symmetry group for the fermions

$$SU(N_f)_L \times SU(N_f)_R \times U(1)_V \times U(1)_A, \tag{2.30}$$

which transform in the following way under the vector and chiral symmetry transformations:

$$\psi_L \to e^{i\theta_L^n F_L^n}\psi, \qquad \bar{\psi} \to \bar{\psi} e^{-i\theta_L^n F_L^n}, \qquad SU(N_f)_L, \tag{2.31}$$

$$\psi_R \to e^{i\theta_R^n F_R^n}\psi, \qquad \bar{\psi} \to e^{-i\theta_R^n F_R^n}\bar{\psi}, \qquad SU(N_f)_R, \tag{2.32}$$

$$\psi \to e^{i\gamma_5\theta}\psi, \qquad \bar{\psi} \to \bar{\psi} e^{i\gamma_5\theta}, \qquad U(1)_A, \tag{2.33}$$

$$\psi \to e^{i\theta}\psi, \qquad \bar{\psi} \to \bar{\psi} e^{-i\theta}, \qquad U(1)_V. \tag{2.34}$$

Where the flavor singlet transformations are omitted as we will be focusing on non-singlet operators in the next chapters; in other works these are considered in probing susceptibility to chiral symmetry such as [34]. In addition to the $SU(N_f) \times SU(N_f)$ symmetry we also include the global vector and axial $U(1)_A$ transformations. Again, the relationship between the right handed and left handed sectors of the $SU(N_f)_L \times SU(N_f)_R$ are one aspect of the chiral symmetry present in the massless limit of the QCD lagrangian.

For $N_f = 2$ the non-singlet generators of flavor transformations become the set of Pauli matrices and the total chiral symmetry can be written as

$$SU(2)_L \times SU(2)_R \times U(1)_A \times U(1)_V. \tag{2.35}$$

The corresponding vector-like chiral transformations are

$$\psi_L \to e^{i\theta_L^n \tau_L^n/2}\psi, \qquad \bar{\psi} \to \bar{\psi} e^{-i\theta_L^n \tau_L^n/2}, \qquad SU(2)_L, \tag{2.36}$$

$$\psi_R \to e^{i\gamma_5\theta_R^n \tau_R^n}/2\psi, \qquad \bar{\psi} \to \bar{\psi} e^{i\gamma_5\theta_R^n \tau_L^n/2}, \qquad SU(2)_R, \tag{2.37}$$

while the global $U(1)$ symmetries remain unchanged. In referring to chiral symmetry typically $U(1)_V$ is omitted as this is a global symmetry associated with baryon number conservation. It is worth noting that "chiral symmetry" refers to both the $SU(2)_L \times SU(2)_R$ and $U(1)_A$ symmetries as both have connection to the chiral condensate.

Specifically the $SU(2)_L \times SU(2)_R$ symmetry, while exact in the massless limit is actually approximate for theories of QCD which consider light degenerate quarks such as $N_f = 2$. In this theory the scale of QCD which is roughly ~ 500MeV in comparison to the physical point up and down quarks (~ 2.2MeV and ~ 4.7MeV respectively) constitutes an approximation to the massless chiral limit in the study of light quark two and three point functions. As such information about the chiral symmetry can be extracted from massive two and three point correlation functions from a series of interpolators which have connections to these underlying symmetries.

2.2.2 Spontaneous Breaking of Chiral Symmetry

$SU(2)_L \times SU(2)_R$ chiral symmetry of the quarks in QCD plays an important role at low temperatures as it connects directly to the mass of the pion. While it is easiest to illustrate this for $N_f = 2$, the arguments are generic and can incorporate N_f degenerate flavors. The spontaneous breaking of chiral symmetry

$$SU(2)_L \times SU(2)_R \to SU(2)_V, \tag{2.38}$$

corrsponding to the set of transformations,

$$\psi \to e^{i\theta_n \tau^n/2}\psi, \qquad \bar{\psi} \to \bar{\psi} e^{-i\theta_n \tau^n/2}, \tag{2.39}$$

can be detected by an order parameter, the chiral condensate $\langle \bar{\psi}\psi \rangle$. The association of the chiral condensate with the breaking of the chiral symmetry largely relates the to the fact that at low temperature the isospin symmetry of both the mesons and hadrons is described by the $SU(2)$ vectorlike symmetry alone, implying the spontaneous breaking of the axial sector of isospin transformations.

As the symmetry is broken spontaneously we expect the presence of a massless Nambu-Goldstone Boson and the presence of an order parameter to detect said broken symmetry. As mentioned above the chrial condensate is such an order parameter which can detect the breaking of the axial sector, consider applying a transformation in $SU(2)_L \times SU(2)_R$

$$\langle \bar{\psi}\psi \rangle \to \langle 0 | \bar{\psi} e^{-i\theta_a \tau^a + i\gamma_5 \phi_b \tau^b} e^{i\theta_a \tau^a + i\gamma_5 \phi_b \tau^b} \psi | 0 \rangle \,, \tag{2.40}$$

it is obvious that the vector symmetry associated with a $SU(2)_L \times SU(2)_R$ leaves the condensate invariant. However, the axial vector symmetry transformation remains; thus when the chiral condensate acquires a non-zero vacuum expectation value axial vector transformations shift the value indicating broken $SU(2)_L \times SU(2)_R$. At finite but high temperatures QCD undergoes a chiral crossover wherein the VeV of the chiral condensate vanishes which would allow the quarks to transform invariantly under the axial vector transformations thereby "restoring" the full vector like chiral $SU(2)_L \times SU(2)_R$. By itself the chiral condensate is one piece of evidence for the spontaneous breaking of chiral symmetry, to fully understand when chiral symmetry is broken we also need to look at the associated Nanbu-Goldstone bosons which result from the SSB.

As the chiral symmetry is approximate for the light quarks the associated Nanbu-Goldstone bosons are actually pseudo Nambu-Goldstone bosons with a mass which is related to the

VeV of the chiral condensate. At energies below the chiral crossover we can construct an effective action for the mesons and show that the $SU(2)_V$ isospin transforms between the three states of the pion π^0 and $\pi^\pm$. Based on this effective action we can model all low energy interactions using chiral perturbation theory; from chiral perturbation theory we can derive the Gell-Mann-Oakes-Renner relation

$$m_\pi^2 = -2\frac{m_u + m_d}{F_\pi^2} \langle \bar{\psi}\psi \rangle , \tag{2.41}$$

which gives us a more or less direct connection between the formation of the pseudo Nambu-Goldstone bosons and the VeV of the chiral condensate. It is therefore, more evident that the relationship between the formation of the pion states at low energies and the breaking of chiral symmetry is intimately connected as the square of the mass of the pions is directly proportional to the expectation of the chiral condensate.

The converse of the previous argument, the restoration of chiral symmetry, is not as straightforward to show; evidence for resotration comes through the chiral condensate and the phase diagram of QCD as well as analysis in the infinite temperature limit. The ability to show this directly at high temperatures in finite temperature QCD is not easily done analytically, analogous to the low energy effective theory from chiral perturbation theory. The most effective means to study chiral symmetry restoration has been from the lattice, as numerical studies of QCD have yielded direct evidence of the chiral crossover and estimations of both the crossover temperature as well as behavior above the transition.

2.2.3 Axial Symmetry and the Quantum Anomaly

As with the chiral $SU(2)_L \times SU(2)_R$ the full symmetries of the Lagrangian in the chiral limit need to be further qualified; in the case of the $U(1)_A$ symmetry, while the Lagrangian remains invariant under transformation, the propagator and associated two and three point functions all fail to retain the same gauge invariance under transformation by $U(1)$. This is known as the Adler-Bell-Jackiw anomaly [35, 36] which explicitly breaks $U(1)_A$ and was originally shown in QED with chiral fermions. This anomaly which is a feature of the quantized theory is actually linearly divergent for a single charged field propagating without a chiral partner field. In addition to this Fujikawa showed that the axial transformation of the Lagrangian modifies the measure of the propagator inducing an anomalous divergence in the axial vector current:

$$\partial_\mu j^\mu(x) = \frac{1}{32\pi^2}\epsilon^{\mu\nu\rho\sigma}\mathrm{tr}[F_{\mu\nu}F_{\rho\sigma}]. \tag{2.42}$$

The quantum anomaly is a low energy effect and thus $U(1)_A$ is broken at a scale below the cutoff of a given theory and thus appears at any energy scale. Additionally, this also implies that the $U(1)_A$ is broken at all scales of QCD and thus makes study of the full chiral symmetry for QCD impossible.

However, there is actually a link between the axial symmetry breaking effect and fluctuation of topological charge Q_T, while the global topological charge is zero local fluctuations of topological charge in the gauge field can be calculated from the topological density of the gauge field

$$Q_T = \int d^4x \frac{1}{32\pi^2}\epsilon^{\mu\nu\rho\sigma}\mathrm{tr}[F_{\mu\nu}F_{\rho\sigma}]. \tag{2.43}$$

The resulting integer charge of Q_T is actually connected to the number left handed and right handed zero modes in the Dirac operator by the Atiyah-Singer index theorem[37, 38],

$$Q_T = n_L - n_R. \tag{2.44}$$

Meaning that the axial anomaly is connected to topological excitations in the gauge field, in the context of QCD these are complex gluonic excitations. These topological gluonic excitations have an effective description as instantons through the associated topological charge and have been shown to break the $U(1)_A$ symmetry [39].

However, in the case of light dynamical quarks such as $N_f = 2$ the topological instanton fluctuations may not play as strong a role and could be suppressed at high temperatures reducing susceptibility to the anomaly and effectively "restoring" the $U(1)_A$ at high temperatures [40, 41, 4, 42, 43, 44] For the light quarks we expect the scale of topological excitations $> 1/T$ and as such the description of $U(1)_A$ remaining broken up to temperatures around the chiral crossover, described by instanton excitations may not be accurate [8, 9, 10, 11].

Chapter 3

Lattice and the Mobius Domain Wall Fermion Operator

To this point we have considered field theories in both the continuum and in Lorentz invariant space-time. As we have mentioned in chapter 2 the approach to studying field theories in the continuum using perturbation theory has had tremendous success for sufficiently weakly coupled theories such as QED and $SU(2)$ electroweak. However, for QCD due to the strong coupling and form of the coupling beta function we find that the low energy interactions, which form the bulk of interactions, as well as, the formation of low energy bound states such as those in the nucleons and mesons are unable to be calculated effectively using perturbative methods. While chiral perturbation theory can form a low energy effective theory describing the exchange of pions as the mediator of interactions, it is not sufficient to study the properties of quarks and mesons. To directly study the properties of quarks and mesons in QCD we need numerical and analytic methods which can study the low energy regime non-perturbatively.

To these ends in this chapter we will cover a short reintroduction to the lattice(following a sketch similar to Rothe [45]), lattice gauge theories and how to propagate chiral symmetry to fermions placed on the lattice. Following this we will discuss the Mobius domain wall fermion, an approximation of the Overlap fermion, which allows us a more or less exact chiral symmetry which is theoretically clean.

3.1 Wick Rotation

In working on the lattice we must transition out of the Lorentz space-time into Euclidean space-time, this not only allows us to simplify our expressions, but also gives us advantages in our method of calculating VeVs more or less directly as expectation values from the spectrum of thermal states in the Hilbert space. Moving forward we will be considering the QCD field theory and lattice field theories in Wick rotated space time $t \to it$. Which takes the path integral to a form analogous to the partition function

$$\langle \varphi(x') | \varphi(x) \rangle = \int \mathcal{D}[\varphi] e^{-S_E}, \tag{3.1}$$

where the S_E is the Euclidean path action:

$$S_E = \int d^4x \mathcal{L}[\varphi(x), \partial_\mu \varphi(x)]. \tag{3.2}$$

Two additional major advantages to using the Wick rotated form of the propagator is the additional use of thermal physics formal tools to analyze the behavior quantum fields, and the biggest advantage: our ability to calculate field theory observably numerically.

One final note about the Euclidean field theory formulation, fundamentally field theories live in a Lorentz invariant space time; studying a Euclidean field theory may not appear at first to be consistent with the original "real" field theory, however, for the Euclidean field theory we have the ability to recover the original field theory by means of analytic continuation to the physical propagator. This is more easily said than done, as direct recovery of the non-Euclidean field theories can be quite nontrivial, although they are accessible mathematically.

3.2 Lattice Discretization

3.2.1 Toy Model for a Scalar Field Theory

Discretization of spacetime in the Euclidean field theory is actually quite straigthforward, by taking all continuous positions to discrete steps scaled by a spacing parameter e.g $x \to na$, we can simply break the action integral into a sum over the space time dimensions written thusly,

$$\int d^4x \to a^4 \sum_n, \tag{3.3}$$

with the corresponding form of the action

$$S_E = a^4 \sum \mathcal{L}[\phi(na), \partial_\mu \phi(na)]. \tag{3.4}$$

Where the covariant derivative is now taken to be a finite difference operator between sites, in the case of a simple scalar field the continuum form of the Lagrangian

$$\mathcal{L}_E = \frac{1}{2}\partial_\mu \phi(x)\partial_\mu \phi(x) + m^2\phi^2(x), \tag{3.5}$$

the covariant derivatives become right-ward and left-ward acting as the derivatives mix sites $n+1$, n and $n-1$ and following units contributes $1/a$. The resulting Lagrangian after discretization,

$$\mathcal{L}_E = \frac{1}{2}a^2 \sum_\mu \frac{1}{a^2}\varphi(na)\Big(\varphi(na+\hat{\mu}a) + \varphi(na-\hat{\mu}a) - 2\varphi(na)\Big) + m^2\varphi^2(na), \tag{3.6}$$

is simply a lattice form of the Klein-Gordon operator for the scalar field with a discrete eigenvalue spectrum based on the discretization of the position $y, x \to m, n$. In moving from (3.5) to (3.6) we assign a lattice unit to the scalar fields

$$\varphi(na) \equiv a\phi(na), \tag{3.7}$$

the mass in the Klein-Gordon operator also has dimensions inverse length and so we will make it unitless by defining

$$M \equiv am, \tag{3.8}$$

making the action explicitly unitless. Now the lattice Klein-Gordon operator can be expressed explicitly as a matrix spanning the configuration space:

$$K_{m,n} = -\sum_{\mu} \Big[\delta_{m+\hat{\mu},n} + \delta_{m-\hat{\mu},n} - 2\delta_{m,n} \Big] + M^2 \delta_{m,n}. \tag{3.9}$$

This form of the Klein-Gordon operator can be inverted by applying a discrete Fourier series over the position space

$$K^{-1}(k) = \sum_{m,n} \Bigg(-\sum_{\mu} \Big[\delta_{m+\hat{\mu},n} + \delta_{m-\hat{\mu},n} - 2\delta_{m,n} \Big] + M^2 \delta_{m,n} \Bigg) e^{ik(m-n)}, \tag{3.10}$$

This yields the inverse Green's function and also gives us the

$$K^{-1}(k) = 4 \sum_{\mu} \sin^2 \left[\frac{ak_\mu}{2} \right] + M^2, \tag{3.11}$$

where k_μ now is written as a physical momentum as opposed to the previously unitless k. Taking $\widetilde{k'_\mu} = 2/a \sin[ak_\mu/2]$ the solution of the Green's function can be written in a familiar manner

$$G(x,y) = a^2 \int_{-\pi/a}^{\pi/a} \frac{d^4 k_\mu}{2\pi^4} \frac{e^{iak_\mu(x/a - y/a)}}{\sum_\mu \widetilde{k'_\mu}^{\,2} + m^2} \tag{3.12}$$

The Green's function derived from the discretized Klein-Gordon operator can be easily shown to converge to the continuum form in the $a \to 0$ limit as $\widetilde{k'_\mu} \to k_\mu$, while the unitless mass contains a^2. The relationship between the two point function and the Green's function contains a $1/a^2$:

$$\langle \phi(x)\phi(y) \rangle = \lim_{a \to 0} \frac{1}{a^2} G(x,y) \tag{3.13}$$

indicating that the lattice form of the non-interacting scalar field theory does indeed describe correct quantum field theory once we return to the continuum field theory.

3.2.2 Computational form of the Propagator

Now that we consider field theories which are no longer in the continuum, we must also understand how this impacts the form of the propagator. In this case we can write out the propagator for out toy model scalar field with some operator O:

$$\mathcal{Z}_O = \frac{1}{\mathcal{Z}_0} \int \mathcal{D}[\varphi(x)] e^{-S_E[\varphi(x)]} O[\varphi(x)]. \tag{3.14}$$

Because the propagator is derived by taking a continuous limit over discrete steps through the phase space or configuration space, when we impose the condition that position and

momenta of the theory are no longer smooth the form of the propagator changes shifts from an integral over the rigged hilbert space representing the infinite states accessible to the field to something of a massive thermal ensemble in a finite but large configuration space. Correspondingly, the path action which was previous also smooth becomes a discrete sum

$$\int d^4x \;\; \rightarrow \;\; a^4 \sum_n, \tag{3.15}$$

$$\int \mathcal{D}[\varphi(x)] \;\; \rightarrow \;\; \sum_\Omega, \tag{3.16}$$

while the path action remains largely the same quantity up to an overall small error, the form of the integral over the continuous set of states becomes a large set of thermal states controlled by a Boltzmann weight. To this end the expectation value associated with the operator listed above can now become a straightforward expectation value over a statistical ensemble:

$$\mathcal{Z}_O = \frac{1}{\mathcal{Z}_0} \sum_\Omega e^{-S_E[\varphi]} O[\varphi] = \frac{1}{N} \sum_{\Omega'} O[\varphi] = \langle O \rangle_{\Omega'} \,. \tag{3.17}$$

Where Ω' is the subset of states in the thermal ensemble which have a non vanishing weight from the Boltzmann factor. Therefore a sufficiently large sample (N) of expectation values in this set of states Ω' can be expected to converge onto the result of the continuum solution to the propagator up to an overall error if there are no artifacts introduced in discretization.

This approach to studying the field theory from the lattice perspective allows us to use this sampling to study non-perturbative theories from using numerical methods. In addition to this we can be assured that the theory remains healthy in the low energy infrared limit as the theory is automatically regularized by the fact that the number of sites n is always finite. While this does mean recovery of infrared results may be fraught in the taking the $n \rightarrow \infty$ and $a \rightarrow 0$ limits we can again expect that the lattice results, if free of artifacts, actually give us solutions of the propagator. In the case of field theories like QCD which cannot be perturbatively examined in the infrared limit due to the catastrophic increase in contributing diagrams the lattice approach offers a siginficant advantage. Likewise the ultraviolet limit of theories is well controlled on the lattice as the higher energy lattice, while very fine, is still fixed to finite spacing between the sites; in such a case even if the lattice has millions of sites the discrete set of states are still thermally regulated and thus well behaved.

3.2.3 Gauge Fields and Fermions on the Lattice

Now that we have had discussion of the changes to the propagator and seen how the path action for a toy model is transformed by discretization, we will focus on the actual description of QCD on the lattice[1]. To this end we introduce the lattice analogue to the continuous gauge field: the gauge link,

$$U_\mu(x) = e^{igaA_\mu(x)}, \tag{3.18}$$

[1]For simplicity, when discussing the lattice spacetime coordinates we will continue using the form of the continuous variables with understanding they are in fact discrete.

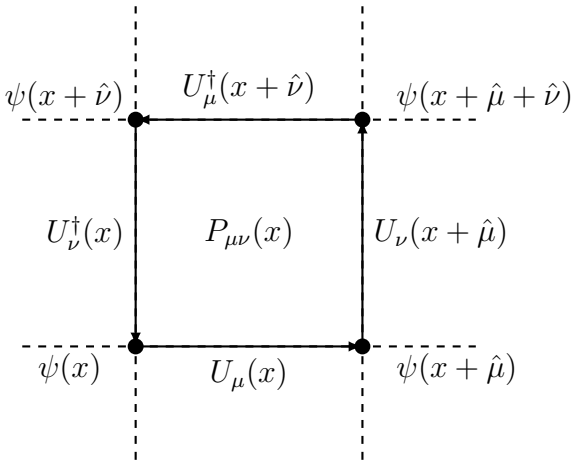

Figure 3.1: An example of the plaquette $P_{\mu\nu}(x)$ with labelled links and fermion spinors representing the relevant quantities in the lattice action.

which transforms in the following way

$$U_\mu(x) \to G(x)U_\mu(x)G(x+\hat{\mu}). \tag{3.19}$$

Unlike the continuous form of the gauge field in which the generators formed the elements of the Lie Algebra of $SU(N)$ the links are the are truly the group elements of $SU(N)$. This means that constructing the analogous expression to mirror the action for the gauge fields is directly constructed from the links themselves.

Because gauge links are directional and represent vector fields on the lattice they have a few special properties, for a single sit there are up to d gauge links which radiate out of a position all of which connect to the adjacent sites in their respective directions. This impacts the gauge transformations above as the link must be transformed at the edges of the link as the link lives between the sites. Due to the links having a directionality, the inverse is equivalent to flipping the direction of the vector associated with the next site e.g.

$$U_\mu^\dagger(x-\hat{\mu}) = U_{-\mu}(x). \tag{3.20}$$

For this reason we can think of the gauge links "flowing" throughout the lattice from left to right and from bottom to top.

For an abelian gauge theory the correspondence between the plaquette and the field strength can be constructed by replacing the derivatives of the vector potentials with finite differences akin to other lattice quantities. The plaquette is smallest unit of the gauge field constructed on the lattice, and the gauge field strength tensor can be expressed from the plaquette in the following way:

$$P_{\mu\nu}(x) = U_\mu(x)U_\nu(x+\hat{\mu})U_\mu^\dagger(x+\hat{\nu})U_\nu^\dagger(x) = e^{ig^2F_{\mu\nu}(x)}, \tag{3.21}$$

plainly seen from the expression of the link (3.18). While this is very easily shown in abelian gauge theories, it is also quite straightfowardly shown in an $SU(N)$ gauge theory. Based on

the form of the plaquette we can apply a simple exponential expansion to recover the form of the continuum gauge field action up to an overall error

$$S_G = \frac{2N}{g^2}\sum_x\sum_P 1 - \frac{1}{2N}\mathrm{tr}\Big[\frac{P_{\mu\nu}(x) + P^\dagger_{\mu\nu}(x)}{2}\Big]. \tag{3.22}$$

The gauge field action is written in the form of the $SU(N)$ theory where the plaquette $P_{\mu\nu}(x)$ is now explicitly path ordered due to the non-commutative nature of the gauge fields in $SU(N)$.

3.2.4 Naive Fermion discretization and the doubling problem

We also can consider a discretization of the fermionic fields, recall that in chapter 2 the fermions are also subject to gauge transformations, on the lattice the fermions retain the typical form of their gauge symmetry

$$\psi(x) \rightarrow G(x)\psi(x), \tag{3.23}$$
$$\bar\psi(x) \rightarrow \bar\psi(x)G^\dagger(x). \tag{3.24}$$

Discretization of the spinors is not quite straightforward as the Lagrangian for the scalar fields, and unlike the toy model we will consider fermions interacting with the gauge fields. This simply means an inclusion of the gauge covariant derivative in the kinetic part of the Dirac operator,

$$S = \int d^4x\bar\psi(x)\not{\mathcal{D}}(x)\psi(x) + m\bar\psi(x)\psi(x). \tag{3.25}$$

Because the inclusion of gauge fields into the lattice action is somewhat more straightforward, as shifting $\partial_\mu \rightarrow D_\mu$ simply requires inserting a link variable; we will describe the doubling problem in the lattice action containing the fermions using the simple non-interacting dirac field equation.

Previously, in the case of the scalar field, discretization has been simply treating the fields as restricted to the sites of the lattice with the continuous variable $x \rightarrow na$. The action was then taken to a simple difference between the fields at neighboring sites. This is seen when we consider that the point x has a difference in sign when approached from the left and right

$$D_\mu\psi(x) = \frac{1}{2}[U_\mu(x)\psi(x+\hat\mu) - U_\mu(x)\psi(x) - U^\dagger_\mu(x-\mu)\psi(x-\hat\mu) + U_\mu(x)\psi(x)]. \tag{3.26}$$

As with the case of the scalar field simply apply the difference between the x and its neighbors, however, for the case of the dirac equation we require that the derivative term is anti-hermitian, thus we introduce a sign difference between the difference from the right as opposed to the difference from the left.

$$S = a^4\sum_x\sum_\mu \frac{1}{2a}\bar\psi(x)\gamma_\mu U_\mu(x)\psi(x+\mu) - \bar\psi(x)\gamma_\mu U^\dagger_\mu(x-\mu)\psi(x-\mu)] + m\bar\psi(x)\psi(x) \tag{3.27}$$

The obvious rescaling choice for the fermions

$$\psi(x) \equiv \frac{1}{a^{3/2}}\psi(x). \tag{3.28}$$

The associated unitless operator matrix which contains spinor indices along with the explicit separation in the position index:

$$K^{\alpha\beta}(x,y) = \frac{1}{2}\sum_{\mu}\gamma_{\mu}^{\alpha\beta}[U_{\mu}(x)\delta_{x+\hat{\mu},y} - \delta_{x-\hat{\mu},y}U_{\mu}^{\dagger}(y)] + \delta^{\alpha,\beta}\delta_{x,y}M \tag{3.29}$$

While this form of the dirac operator looks analogous to our scalar field toy model from sec 3.2.1 and is seemingly innocuous, we must examine the associated two-point function. We will ignore the link terms in the gauge covariant dirac operator as the leading order free fermion behavior will show what our discretization has done to the fermions in our propagator. Upon expanding this as a fourier series in the four momenta we can extract a momentum term which converges to the linear dispersion as $a \to 0$.

$$K^{\alpha\beta}(p) = \sum_{x,y} K^{\alpha\beta}(x,y)e^{ip(x-y)} \tag{3.30}$$

$$= \sum_{x,y}\left[\frac{1}{2}\sum_{\mu}\gamma_{\mu}^{\alpha\beta}[\delta_{x+\hat{\mu},y} - \delta_{x-\hat{\mu},y}] + \delta^{\alpha,\beta}\delta_{x,y}M\right]e^{ip(x-y)} \tag{3.31}$$

$$K^{\alpha\beta}(p) = a\sum_{\mu} i\gamma^{\mu}\frac{1}{a}\sin(p_{\mu}a) + m \tag{3.32}$$

In the argument of the sine function the unitless momentum is re-rescaled to correspond to the physical momentum. Introducing

$$\widetilde{p}_{\mu} = \frac{1}{a}\sin(p_{\mu}a), \tag{3.33}$$

allows us to write the two point function directly as the Green's function corresponds to the two-point function with the square of our rescaled field units:

$$\langle\bar{\psi}(x)\psi(y)\rangle = \lim_{a\to 0}\left(\frac{1}{a^{3/2}}\right)^2 K^{-1}_{\alpha,\beta}(x,y). \tag{3.34}$$

If we consider the form of the two point function for the fermions in the continuum limit it becomes very quickly obvious that the dirac operator, in being discretized, has introduced several additional artifacts once placed on the lattice see fig. 3.2 for details,

$$\langle\psi_{\alpha}(x)\bar{\psi}_{\beta}(y)\rangle = \lim_{a\to 0}\int_{-\pi/a}^{\pi/a}\frac{d^4p_{\mu}}{(2\pi)^4}\frac{[\sum_{\mu} -i\gamma^{\mu}\widetilde{p}_{\mu}^2 + m]_{\alpha\beta}}{\sum_{\mu}\widetilde{p}_{\mu} + m^2}e^{ip_{\mu}(x-y)}. \tag{3.35}$$

The low momentum mode which we expect to form the ground state consistent with the dispersion relation shown in 3.2(b), is contaminated by the presence of additional low momenta which are present at the edges of the Brilluon zone. In the continuum limit, as said above these states diverge as the edges of the Brilluon zone expand to an infinite limit; the presence of the doublers in the Green's function for our two point function are connected to all of the four momenta for which the sine function is zero. Thus for a 4d theory we have the

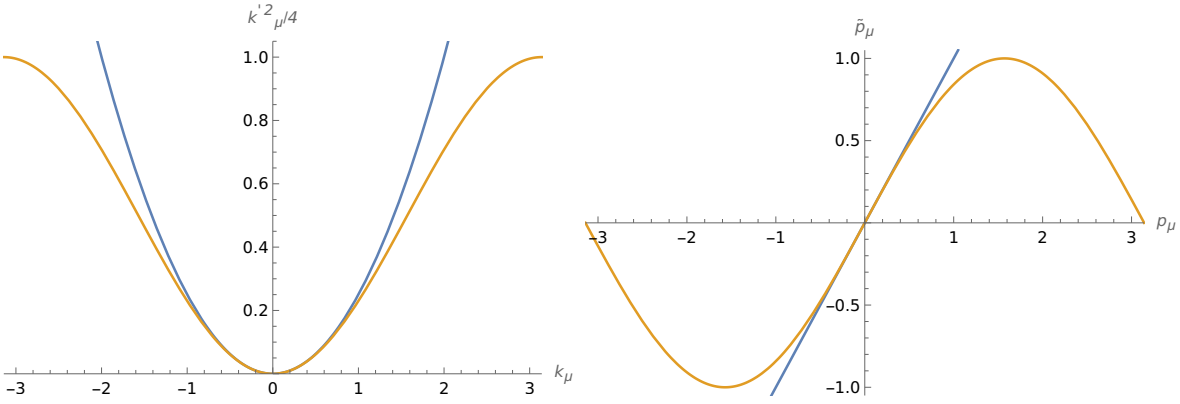

(a) (b)

Figure 3.2: In 3.2(a) the re-scaled dispersion of the scalar field is plotted in the Brilluon zone $[-\pi/a, \pi/a]$. As we can see from the graph, approximation of the field behavior for $\widetilde{k'_\mu} \approx k_\mu$ is localized around the origin, therefore as $a \to 0$ the approximation becomes exact consistent with the argument from 3.2.1. While the plot in 3.2(b) has $p_\mu \approx \widetilde{p_\mu}$ near the origin, there are also two addition points which also have the same momentum located at $\pm\pi/a$; this means that we get couplings to momenta which diverge as we take the lattice spacing to zero. This introduces erroneous phase shifted low momenta which break the continuum convergence for the fermionic theory, these doublers scale with dimension as 2^d.

one momentum which corresponds to the groundstate and fifteen additional artifact states which do not exist in the continuum theory.

There is actually quite a deep reason that we find doublers in the theory of fermions on the lattice, which is critically connected to the presence of the Adler Bell Jackiw anomaly in QED [36, 35]. From chapter 2 we know that in the massless limit the Dirac operator has the property

$$\{D, \gamma_5\} = 0, \tag{3.36}$$

and the fermions transform under a global axial symmetry

$$\psi \rightarrow e^{i\gamma_5\theta}\psi, \tag{3.37}$$

$$\bar{\psi} \rightarrow \bar{\psi}e^{i\gamma_5\theta}. \tag{3.38}$$

We assume that this property also holds for the lattice as the lattice Dirac operator in the massless limit does appear to share this property; however, this assumption, which may be seen as natural, is incorrect because the lattice regularization assures that any symmetry like the axial symmetry has a conserved current at all spacings. According to [46], the formation of doublers arises from the tension between the presence of the anomaly, which appears a low momentum, with the apparently anomaly free regularization of the lattice. The way that this is occurs can be seen by breaking up the regions of the hypercubic momentum into their axial charge sectors by restricting the range of integration in (3.35) to $[\pi/2a, -\pi/2a]$ and introducing $\delta\bar{p}_\mu$

$$\delta_{\bar{p}_\mu} \equiv e^{i\bar{p}_\mu}. \tag{3.39}$$

$\bar{p}_\mu$ is not a range of momentum like p_μ or $\widetilde{p}_\mu$ but a choice in the pole momentum configuration for edge states shown in the middle column of Tab.3.1. These pole coordinates induce a phase in the overall integral which cannot converge upon taking the continuum limit, while the pole at $\bar{p}_\mu = (0,0,0,0)$ has no such phase and may converge to the continuum limit without problem,

$$\langle \psi_\alpha(x)\bar{\psi}_\beta(y)\rangle = \sum_{\bar{p}_\mu} e^{i\frac{\bar{p}_\mu}{a}(x-y)} \int_{-\pi/2a}^{\pi/2a} \frac{d^4p_\mu}{(2\pi)^4} \frac{[\sum_\mu -i\delta_{\bar{p}_\mu}\gamma^\mu \widetilde{p}_\mu + m]_{\alpha\beta}}{\sum_\mu \widetilde{p}_\mu + m^2} e^{ip_\mu(x-y)}. \tag{3.40}$$

The phase factor associated with the spatial coordinates allows the two point function to be written in terms of a local axial transformation based on the four momenta sector. The product of the gamma matrix and the four momenta sector delta function can be expressed as a similarity transformation of the gamma matrix by the tensor $\mathcal{T}_{\bar{p}_\mu}$ which changes rank based on the four momentum sector:

$$\delta_{\bar{p}_\mu}\gamma^\mu = \mathcal{T}_{\bar{p}_\mu}\gamma^\mu\mathcal{T}^{-1}_{\bar{p}_\mu}, \tag{3.41}$$

transformations are listed in 3.1. Where the tensors $\mathcal{T}_{\bar{p}_\mu}$ can actually be treated as a pseudo-symmetry

$$S_F^{\alpha,\beta}(x,y) = a^3 \sum_{\bar{p}_\mu} e^{i\frac{\bar{p}_\mu}{a}x}\mathcal{T}_{\bar{p}_\mu}\left[\int_{-\pi/2a}^{\pi/2a} \frac{d^4p_\mu}{(2\pi)^4} \frac{[\sum_\mu -i\gamma^\mu \widetilde{p}_\mu + m]_{\alpha\beta}}{\sum_\mu \widetilde{p}_\mu + m^2} e^{ip_\mu(x-y)}\right]\mathcal{T}^{-1}_{\bar{p}_\mu} e^{-i\frac{\bar{p}_\mu}{a}y}, \tag{3.42}$$

in fact, this same transformation

$$V_{\bar{p}_\mu}(x) = e^{i\frac{\bar{p}_\mu}{a}x}\mathcal{T}_{\bar{p}_\mu}, \tag{3.43}$$

can also be applied to the original action which is invariant under such transformations. This set of transformations correspond to the chiral transformation in 2.

In fact, these additional phases arise from the regularization of the lattice, as the lattice regularizes the fermions in such a way as to assign cancellation of axial charge to each low momentum state seen from the associated charge assignment column in Table 3.1. Based on this, there is an even charge assignment with 8 states having -1 and another 8 having +1, leading to the cancellation of the anomaly consistent with the lattice regularization condition of preserving the axial current for any a. This is physically inconsistent, as the ABJ anomaly is known to be broken by quantum fluctuations and actually has a divergent current.

3.3 Wilson-Fermions and extension of the Dirac operator on the Lattice

To have a physically consistent theory for fermions on the lattice the doublers need to be eliminated to recover the proper anomaly in the continuum amongst other properties which may also be eliminated by the lattice regularization condition. The famous Nielsen-Ninomiya no-go theorem [47, 48, 49] actually lays out criteria for which a regulated theory produces doublers; for the lattice, as the theory is already regularized in attempting to introduce chiral

$\mathcal{T}_{\bar{p}_\mu}$	Pole Coordinates($\bar{p}_\mu$)	Chiral Charge	N_{pole}
$\mathbb{1}$	for (0,0,0,0)	+1	1
$\mathcal{T}_\mu = \gamma^\mu\gamma_5$	states with $(\pi,0,0,0)$	-1	4
$\mathcal{T}_{\mu\nu} = \gamma^\mu\gamma_\nu$	states with $(\pi,\pi,0,0)$	+1	6
$\mathcal{T}_{\mu\nu\lambda} = \gamma^\mu\gamma_\nu\gamma_\lambda\gamma_5$	states with $(\pi,\pi,\pi,0)$	-1	4
$\mathcal{T}_{\mu\nu\lambda\rho} = \gamma_5$	for (π,π,π,π)	+1	1

Table 3.1: The axial charge for various four momenta in the 4d theory of fermions on the lattice.

symmetry consistent with (3.36) we get doublers. However, if we break the chiral symmetry we can produce a lattice theory with fermions that eliminates the doublers. Beginning with action already in momentum space

$$S = \sum_{x,y} \int \frac{d^4p}{(2\pi)^4} \bar{\psi}(-p) \Big(\sum_\mu i\gamma^\mu \sin[p] + M \Big) \psi(p) e^{ip(x-y)}, \tag{3.44}$$

the problem with the doublers is that the states which form the artifacts are degenerate with the pole at $(0,0,0,0)$. Coupling the states with $\sin(p) = 0$ but with non-zero momentum configurations to the mass will raise the doubler states but leave the proper zero momentum pole,

$$S = \sum_{x,y} \int \frac{d^4p}{(2\pi)^4} \bar{\psi}(-p) \Big(\sum_\mu i\gamma^\mu \sin[p] + M + r\sum_\mu 1 - \cos[p] \Big) \psi(p) e^{ip(x-y)}. \tag{3.45}$$

This new term eliminates the doublers but breaks the chiral symmetry as the $M \to 0$ limit is no longer invariant under chiral transformation. Examining the Green's function for the fermions

$$S_F(p) = \frac{-i\gamma^\mu \sin[p] + M(p)}{\sin^2[p] + M^2(p)} \quad \text{where} \quad M(p) = M + r\sum_\mu 1 - \cos[p], \tag{3.46}$$

in the continuum limit $a \to 0$ this converges to the continuum Green's function properly. This term modifying the mass is known as the Wilson term, and while it breaks the chiral symmetry on the lattice, it does eliminate doublers while retaining the proper chiral symmetry in the continuum theory. With the Wilson term we can place the fermions on the lattice, but we no longer have a full chiral theory on the lattice. The global chiral symmetry is explicitly broken to

$$SU(N_f)_V \times U(1)_V. \tag{3.47}$$

Although the explicitly broken chiral symmetry of the Wilson fermions is correct below the chiral crossover, for the purposes of studying chiral symmetry restoration and high temperature phenomena related to emergent symmeteries from the lattice directly the Wilson term is insufficient.

3.3.1 Ginsparg-Wilson Fermions

In formulating a new Dirac like operator we would like to retain the lifting of the doublers from the Wilson fermions while also avoiding explicitly breaking the chiral symmetry outright. The resolution to this is to extend the Dirac operator in the fermion action to incorporate the Wilson term while also maintaining the anticommutivity property of the original covariant derivative operator (3.36) in the $a \to 0$ and $m \to 0$ limits. The core of this extension will rely on the anticommutation relation

$$\{D, \gamma_5\} = aDR\gamma_5 D \tag{3.48}$$

R is included as a parameter and sometimes as an additional matrix for largely formal reasons, but typically is set to 1 or $1/m_0$ depending on the context. This anticommuting behavior follows our demand for a chirally symmetric theory as $\{D, \gamma_5\} \to 0$ as $a \to 0$ and $m \to 0$. While the lattice action is not chirally symmetric by construction we do have chiral symmetry emerge not through choice of a particular operator but for all classes of operators subject to the anticommutator.

There is an effective choice of the operator which has a limit that eliminates species doubling in a certain regimes of masses, while also allowing convergence onto a chiral symmetry in the continuum. This operator is called the Overlap operator[50, 51, 52] and is defined as:

$$D_{ov} = \frac{m_0}{a}\left(1 + \frac{D_W(-m_0)}{\sqrt{D_W(-m_0)^\dagger D_W(-m_0)}}\right), \tag{3.49}$$

where $D_W(-m_0)$ is the Wilson-Dirac operator with negative mass :

$$D_W(-m_0) = \frac{1}{2}\not{\mathcal{D}} + \frac{1}{2}aD^2 - \frac{m_0}{a}. \tag{3.50}$$

Crucially the Overlap operator requires that this form of the Wilson operator satisfy a few properties, using the anticommutator for D we can show these required properties:

$$\{D, \gamma_5\} = \gamma_5 D + D\gamma_5 = aD\frac{\gamma_5}{m_0}D \tag{3.51}$$

Introducing the full form of the Overlap operator and dividing both sides by m_0/a and using $X = D_W(-m_0)$:

$$\begin{aligned}
2\gamma_5 + \frac{\gamma_5 X}{\sqrt{X^\dagger X}} + \frac{X\gamma_5}{\sqrt{X^\dagger X}} &= \left(1 + \frac{X}{\sqrt{X^\dagger X}}\right)\left(\gamma_5 + \frac{\gamma_5 X}{\sqrt{X^\dagger X}}\right) \\
2\gamma_5 + \frac{\gamma_5 X}{\sqrt{X^\dagger X}} + \frac{X\gamma_5}{\sqrt{X^\dagger X}} &= \gamma_5 + \frac{X\gamma_5 + \gamma_5 X}{\sqrt{X^\dagger X}} + \frac{X\gamma_5 X}{X^\dagger X} \\
2\gamma_5 &= \gamma_5 + \frac{X\gamma_5 X}{X^\dagger X}
\end{aligned} \tag{3.52}$$

To produce the equality in (3.52) we can show that X is subject to the condition $\gamma_5 X \gamma_5 = X^\dagger$.

The removal of doublers is now contingent on our choice of mass m_0. For $0 < m_0 < 2$ doublers are eliminated while they return for $m_0 > 2$. For $m_0 < 0$ all fermions are massive and we have no massless fermions which mean our chiral symmetry is unable to be recovered.

There is an additional and important property that we can also see from the Ginsparg-Wilson relation which impacts the form of chiral symmetry present on the lattice, if we look again at (3.51) we can identify a quantity which anticommutes with the overlap operator

$$D\gamma_5(1-\frac{1}{2}aD)+\gamma_5(1-\frac{1}{2}aD)D=\{D,\gamma_5(1-\frac{1}{2}aD)\}=0 \tag{3.53}$$

Implying that the term $\gamma_5(1-1/2aD)$ is a modified form of the chiral symmetry, which is exact on the lattice. For the lattice we would like to also check that the action is invariant under the modified chiral symmetry transformations

$$\psi(x) \rightarrow e^{i\phi\gamma_5(1-\frac{1}{2}aD)}\psi(x) \tag{3.54}$$

$$\bar{\psi}(x) \rightarrow \bar{\psi}(x)e^{i\phi\gamma_5(1-\frac{1}{2}aD)} \tag{3.55}$$

In the limit $m \rightarrow 0$ if this modified transformation is a chiral symmetry, then transformation of the fermions (3.54) and (3.55) should find no change to the action. The easiest way to test this is by invoking $\delta S = 0$ by small variations in the chiral transformation of the Dirac spinors.

$$\begin{aligned}\delta S &= \sum_x i\epsilon\bar{\psi}\left[1-\frac{1}{2}aD\right]\gamma_5 D\psi + i\epsilon\bar{\psi}D\gamma_5\left[1-\frac{1}{2}aD\right]\psi \\ &= i\epsilon\sum_x \bar{\psi}[\gamma_5 D + D\gamma_5]\psi - \bar{\psi}\left(\frac{1}{2}aD\gamma_5 D + \frac{1}{2}aD\gamma_5 D\right)\psi \\ &= i\epsilon\sum_x \bar{\psi}\left[\{D,\gamma_5\} - aD\gamma_5 D\right]\psi\end{aligned}$$

So our modified chiral transformation is indeed a symmetry of the action at $m = 0$ indicating that our Ginsparg-Wilson relation does preserve a form of chiral symmetry on the lattice.

The Ginsparg-Wilson relation is quite generic and so there are a number of possible operators we can produce that will preserve this modified form of chiral symmetry. The Overlap operator is one possible choice of operators but it is actually derived from the form of a $5D$ operator, which can be seen by writing down the alternate form of the overlap operator:

$$D_{ov} = \frac{1+m}{2} + \frac{1-m}{2}\gamma_5 \mathrm{sgn}(H). \tag{3.56}$$

H is a more generic kernel operator which is constructed from a proportion of the $4D$ Wilson operator $D_W(-M)$.

Using the Overlap operator we can do simulations of lattice QCD with an exact form of chiral symmetry, and previous work done in the 1990s and 2000s made extensive use of the Overlap operator in lattice studies. However, this does come with some trade offs as there are some technical hurdles which make Hybrid Monte Carlo slower compared, with say, the Wilson operator.

The key issue which slows simulation with the Overlap operator is inversion of the operator itself; therefore, it makes sense to introduce an approximation that simplifies inversion and reduces the compute time while approximating the Ginsparg-Wilson relation.

3.3.2 Domain Wall Fermions

For the free fermion field we will make an extension of the dimension for the theory to $d = 5$, in the case of the the fifth dimension we will not be treating it as an entirely full degree of freedom save for making some modifications to the dirac operator [53].

In the last section we considered the Ginsparg-Wilson relation, and saw that while it preserves a form of chiral symmetry for fermions on the lattice, it is a non-local form which depends explicitly on the Wilson-Dirac operator. As the Ginsparg-Wilson relation is defined generically, we may be able to produce an operator which has a more conventional form of the chiral symmetry. In the case of the domain wall we will actually impose the following transformations on the fermions:

$$\psi(x,s) \rightarrow e^{i\theta^a(s)\tau^a/2}\psi(x,s), \tag{3.57}$$
$$\bar{\psi}(x,s) \rightarrow \bar{\psi}(x,s)e^{-i\theta^a(s)\tau^a/2}, \tag{3.58}$$

where s is the position along the fifth dimension. $\theta(s)$ is actually a piece wise defined function which flips sign at the halfway point of the extension into the fifth dimension,

$$\theta(s) = \begin{cases} \theta^a & (1 < s < N_s/2), \\ -\theta^a & (N_s/2 < s < N_s). \end{cases} \tag{3.59}$$

This is done to introduce a step function like behavior in the fermions mass which now depends on the position along the fifth dimension. As the above transformations (3.58) (3.57) appear to behave like the chiral transformations in the continuum, we can construct a "quark" spinor $q(x)$, which has both a right handed and left handed dirac fermion component

$$q(x) = P_L\psi(x,0) + P_R\psi(x,L_s), \tag{3.60}$$

the quark state is now an interpolated spinor which can be chirally transformed similar to the dirac spinors in the continuum

$$q_L(x) \rightarrow e^{i\theta^a_L\tau^a_L/2}q_L(x), \tag{3.61}$$
$$\bar{q}_L(x) \rightarrow \bar{q}_L(x)e^{i\theta^a_L\tau^a_L/2}, \tag{3.62}$$
$$q_R(x) \rightarrow e^{i\theta^a_R\tau^a_R/2}q_R(x), \tag{3.63}$$
$$\bar{q}_R(x) \rightarrow \bar{q}_R(x)e^{i\theta^a_R\tau^a_R/2} \tag{3.64}$$

However, this would also appear to imply that we have four fermion fields between $q(x)$ and $\bar{q}(x)$, as the new quark field is composed of interpolated left and right handed spinors. The remedy to this is in the form of the domain-wall fermion action, based on the form of the quarks we get a left and right handed projection of the "mass" which is associated with the boundary walls of the fifth dimensional extension

$$\begin{aligned} S_{DWF} &= \sum_x m\Big[\bar{\psi}(x,1)P_R\psi(x,N_s) + \bar{\psi}(x,N_s)P_L\psi(x,1)\Big] \\ &+ \sum_s\Big[\sum_\mu \bar{\psi}(x,s)(P_{L,\mu}U_\mu(x)\psi(x+\hat{\mu},s) + \bar{\psi}(x,s)P_{R,\mu}U^\dagger_\mu(x-\hat{\mu})\psi(x-\hat{\mu},s)\Big] \\ &+ \sum_s \bar{\psi}(x,s)(1-\hat{M})\psi(x,s) - \bar{\psi}(x,s)P_L\psi(x,s+1) + \bar{\psi}(x,s)P_R\psi(x,s-1) \end{aligned} \tag{3.65}$$

it is important to note that the fifth dimension is not periodic like the other four dimensions; in fact, the advantage of this is that due to the mass coupling in the first term the left and right handed fermions live on the boundaries of the fifth dimensional bulk. With the difference between the chiral $q(x)$ and its mirror partner located on the boundary if we take the limit $N_s \to \infty$ the chiral symmetry of $q(x)$ becomes an exact symmetry. However, in practice we must fix to some finite extent sufficient to produce a "good" chiral symmetry for the domain wall fermion operator. In fact, due to the finite extent of the fifth dimension there is mixing between the forward and backward propagating vector like symmetries (3.58) and (3.57) which creates a residual mass artifact which according to [22] is connected to the reverse lattice derivative of the axial current A^a_μ:

$$\triangle^-_\mu A^a_\mu = 2mP^a + 2J^a_5, \tag{3.66}$$

where P^a is the pseudo-scalar density drawn form the Ward-Takahashi identity. This is used to extract the residual mass by taking the proportion of the expectation value between the axial current in the fifth dimension J^a_5 and the aforementioned pseudoscalar density. In this case we define this axial current at the midpoint $N_s/2$ of the total finite extent in 5D. There is an additional form of m_{res} which can be cast as invariant of the dependence directly on the pion mass far from the source point which incorporates the domain wall operator:

$$m_{res} = \frac{\langle \mathrm{Tr}[(D^{-1})^\dagger \triangle D^{-1}] \rangle}{\langle \mathrm{Tr}[(D^{-1})^\dagger D^{-1}] \rangle}, \tag{3.67}$$

D^{-1} is the massive domain wall operator which is the 4D effective overlap operator inverted

$$D^{-1} = \frac{1}{1-m}((D_{DW}(m)^{-1}) - 1). \tag{3.68}$$

In the form above the denominator corresponds to the expectation values of the psuedoscalar density while the numerator term has a defect from the Ginsparg-Wilson relation. In this case the defect is fixed around the mid point coinciding with the point at which we have fixed the axial current. Like the denominator this term simply corresponds to the J^a_5 current term, and thus we have a state invariant form for the residual mass described by the 5D domain wall operator itself.

While the fifth dimensional theory may seem scary, it is largely bypassed by extracting the 4D theory from one boundary of the theory, typically we choose the right handed field which is located on the boundary at the $s = 1$ endpoint. This choice also results in a positive mass term which will also give use the correct behaviors for the fermions and allow us to take the chiral limit of the theory.

3.3.3 Mobius Domain Wall Fermions

So now that we know the domain wall fermions can be used to produce a correct chiral symmetry we would like to fit this back into the form of the overlap operator and examine how this particular operator can simplify the necessary inversions of the overlap operator. To do this we will rewrite the domain wall operator in a slightly more generalized form,

beginning with the matrix form of the operator which is an $L_s \times L_s$ entry matrix

$$D_{DWF} = \begin{bmatrix} D & -P_L & 0 & & \dots & mP_R \\ -P_R & D & -P_L & 0 & \dots & 0 \\ 0 & -P_R & D & -P_L & & \vdots \\ \vdots & 0 & \ddots & D & \ddots & \vdots \\ \vdots & \vdots & \ddots & \ddots & \ddots & -P_L \\ mP_L & 0 & \dots & 0 & P_R & D \end{bmatrix}. \tag{3.69}$$

The form of this matrix may be diagonalized by decomposition of a block diagonal form which is derived by a series of matrix multiplications [54, 55]. In this case it can be be made to correspond to a reduced 4D operator by Pauli-Villars subtraction resulting in the Neuberger form of the 4D overlap operator:

$$D_{ov} = \frac{1+m}{2} + \frac{1-m}{2}\gamma_5 \text{sgn}(H) \tag{3.70}$$

This is another subtlety of the overlap operator form, the sign function is hard to calculate in and of itself as the form of the function changes with choice in the kernel H. Precise knowledge in the form of the sign function is hard and there are many ways to approximate the form of the behavior either through series expansions or directly through functional approximation. In this work we depend on the latter choice by approximating $\text{sgn}(H) \sim \tanh(L_S \tanh^{-1}(H))$. Which will be made a bit more clear after showing the choice of kernel related to the form of the generalized domain wall fermions, this choice of kernel will give us what are call *mobius domain wall fermions*.

To arrive at the form of the mobius domain wall fermions we need to generalize the domain wall operator a bit, based on the diagonal argument we will introduce an algebraic expansion

$$D_+ = a_s(1 + b_s D_W), \tag{3.71}$$
$$D_- = a_s(1 - c_s D_W), \tag{3.72}$$

we can use the forms of these to produce an algebraic operator which comes in powers of the fifth dimensional position s

$$D^s = (D^s_-)^{-1} D^s_+. \tag{3.73}$$

In the case of the domain wall fermion $c_s = 0$ uniformly, but to get a set of constants which do not explicitly depend on the position in the fifth dimension we will again perform a decomposition of the generalized domain wall fermion operator by multiplying first $D_- {D_{GDW}}^2$

$$D_- D_{DW} = \begin{bmatrix} D^1_+ & D^1_- P_- & 0 & & \dots & -mD^1_- P_+ \\ D^2_+ P_+ & D^2_+ & D^2_- P_- & 0 & \dots & 0 \\ 0 & D^3_- P_+ & D^3_+ & D^3_- P_- & & \vdots \\ \vdots & 0 & \ddots & D^4_+ & \ddots & \vdots \\ \vdots & \vdots & \ddots & \ddots & \ddots & D^{L_s-1}_- P_- \\ -mD^{L_s}_- P_- & 0 & \dots & 0 & D^{L_s}_- P_+ & D^{L_s}_+ \end{bmatrix}. \tag{3.74}$$

[2]For the chiral projection operator we relabel these to plus and minus to match signs on the operator D. $P_+ = P_R$ and $P_- = P_L$ in the case of the generalized domain wall operator.

Decomposition of this form of the generalized domain wall fermion to a transfer matrix is somewhat technical, but can be done in the same manner as the standard domain wall fermions. The form of the transfer matrix is noteworthy as this is where we explicitly make the choice over the form of the kernel and the approximation of the step function:

$$T_s^{-1} = \left[1 + \gamma_5 \frac{1 + (b_s + c_s)D_W}{2 + (c_s - b_s)D_W}\right]^{-1} \left[1 + \gamma_5 \frac{1 + (b_s + c_s)D_W}{2 + (c_s - b_s)D_W}\right]. \tag{3.75}$$

Here we can redefine the constants $\alpha_s b = b_s + c_s$ and $c = b_s - c_s$, these now allow us to define the kernel in the transfer matrix,

$$T_s^{-1} = \frac{1 + \alpha_s H}{1 - \alpha_s H}. \tag{3.76}$$

Making the choice to impose that the transfer matrix approximates the overlap operator means choosing constants and expanding the transfer matrix as a product. We make a straightforward choice of $b = 2, c = 0$ the kernel $H \to H_M$, for approximation of the sign function by a hyperbolic tangent we consider direct multiplication of the transfer matrix as a simple gemometric series

$$\mathrm{sgn}(H_M) = \frac{1 - \left(\frac{1-H}{1+H}\right)^{L_s}}{1 + \left(\frac{1-H}{1+H}\right)^{L_s}}, \tag{3.77}$$

in this case the approximation by tanh looks quite simple. However, there are competing schemes for the approximation to the sign function in the Neuberger form of the Overlap Operator such as optimal domain wall fermions [56], or Shamir's approximation [57]. The difference being the choices in coeffficients and assumptions of the form for expansion of the transfer matrix, each offers different regimes of precision for capturing low eigenmodes in the operator but at the cost of numerical intensity.

As with the previous section this defines the 5d version of the operator from which there is an approximate form for which we can recover the 4d overlap operator so the form of the new mobius domain wall fermion operator is identical to the form of (3.70) but now $\mathrm{sgn}(H) \to \epsilon(H)$ where $\epsilon(H)$ is the approximated form of the sign function based on our choice in the kernel and expansion of the transfer matrix. Stated again for the sake of completeness the overlap operator for the mobius domain wall fermions is expressed as follows:

$$D_{ov} = \frac{1 + m}{2} + \frac{1 - m}{2}\gamma_5 \tanh[L_s \tanh^{-1}(H_M)], \quad \text{where} \quad H_M = \frac{\gamma_5 D_W}{2 + \gamma_5 D_W}. \tag{3.78}$$

In this form L_s is the full extent of the sites in the fifth dimension. As for the residual mass originating from the form of the domain wall operator, the mobius domain wall operator actually increases the suppression of the lattice artifact making the chiral symmetry a bit more exact.

For sufficiently long extents in the fifth dimension the residual mass which weakens the chiral symmetry is very mild and allows us to preserve a more or less exact chiral symmetry on the lattice. This has a massive advantage as the methods for analysis is theoretically clean

and so we can study symmetries of quarks through differences between partners correlation functions related to chiral symmetry transformations. This was something we may have done with the overlap operator alone, however, the benefit of approximation of the overlap operator compared with the mildness of the symmetry breaking by way of the residual mass offers us a more efficient numerical approach. There is also the added benefit of removing additional artifacts which may appear based on the method of choice for eliminating doublers on the lattice, which in the case of staggered fermions does in fact introduce an at this point well known artifact in which the scalar meson channel converges to a forbidden decay channel which has a mass of twice the pion. Due to the treatment of the symmetry in the mobius domain wall formulation, we do not suffer from such an artifact giving us some ability to study the low temperature behaviors of the scalar meson below the critical temperature for chiral symmetry restoration.

Chapter 4

Mesonic Correlation lengths in High T QCD

As we cannot directly study quarks since they are confined within hadronic and mesonic bound states looking at symmetries and properties of these bound states in QCD is dependent on studying the properties of two and three point correlations functions. Hence we require correlation functions as a well defined quantity to study generic properties of the fields overall. In particular we will focus on the meson two point correlator to study the thermal properties of mesons as well as their symmetries with respect to finite temperature QCD.

4.1 Finite Temperature on the lattice

On the lattice we have a few parameters which we can use to control the energy scale of the physics of interest. As the renormalized coupling can be made a function of the lattice spacing, we can set the scale of physics by making modifications to the lattice and thus control the scale of energy for the physics. The coupling and the lattice spacing are inversely proportional and thus as we attempt to increase the energy of our lattice theory we shrink the lattice. Instead we would like to increase the energy scale of the physics without shrinking the lattice spacing for which we introduce temporal compactification

$$T = \frac{1}{aN_t}, \tag{4.1}$$

where the energy scale of the lattice is described as temperature by varying either the lattice spacing (through coupling or anisotropy), or directly by change the number of sites along the temporal extension. As we would like to maintain a single coupling, and therefore a uniform lattice spacing, we will consider lattices of different temporal extensions as our control on the temperature.

For our path actions(and later correlators) this substitution is simply swapping

$$\int_{-\infty}^{\infty} dt \to \int_{0}^{\beta} d\tau \quad \text{where} \quad \beta = \frac{1}{T}, \tag{4.2}$$

with the introduction of temperature through the lattice anisotropy the Euclidean time propagator now can be shown to directly correspond with the thermal partition function.

From this perspective we can actually treat all of the field observables as statistical quantities derived from the partition function, this does give us the critically important ability to perform importance sampling via the monte carlo method. While we have many theoretical tools to study field theories analytically strongly coupled theories like QCD have correlators and vacuum expectation values which are difficult to do by hand. In contrast to this our lattice treatment offers the the ability to derive observables and correlators from statistical sampling which we can expect, for sampling with sufficient statistics, actually captures the groundstate of observables in the field theory.

4.2 Mesonic Correlators

The primary quantity we will focus on will be the correlation function made from the quark bilinear function

$$O(x) = \bar{q}(x)\gamma_\mu \otimes F^a q(x). \tag{4.3}$$

Where the dirac spinor is rerepresented as a "quark" since we will be primarily looking at QCD with degenerate up and down quarks. Recall the number of flavors also behaves as an additional $SU(N)$ global symmetry, and in the case of $N_f = 2$ where the flavors are mass degenerate, the flavor generators F^a becomes the Pauli matrices. The form of the interpolator seen above actually can be rewritten generically in terms of four "channels"

$$\begin{aligned} S^a &= \bar{q}F^a q, & (4.4)\\ PS^a &= \bar{q}\gamma_5 F^a q, & (4.5)\\ V^a_\mu &= \bar{q}\gamma_\mu F^a q, & (4.6)\\ A^a_\mu &= \bar{q}\gamma_5\gamma_\mu F^a q, & (4.7) \end{aligned}$$

The S^a and PS^a operators are scalar operators and can be thought of as condensates, as well as interpolators for particle. V^a_μ and A^a_μ represent both represent currents as well as particle interpolators. In addition to these we can consider a pair of tensor operators:

$$\begin{aligned} X^a_{\mu\nu} &= \bar{q}\gamma_{[\mu}\gamma_{\nu]}F^a q & (4.8)\\ T^a_{\mu\nu} &= \bar{q}\gamma_5\gamma_{[\mu}\gamma_{\nu]}F^a q & (4.9) \end{aligned}$$

where the $\gamma_{[\mu}\gamma_{\nu]} \equiv \gamma_\mu\gamma_\nu - \gamma_\nu\gamma_\mu$. For isotropic lattices typically the set of operators S, PS, V_μ, A_μ and $T_{\mu\nu}$ are the full extent of available symmetry transformations. However, for a time compacted lattice the axial transformation of $T_{\mu\nu}$ does appear to behave as a unique operator leading to an axial partner operator $X_{\mu\nu}$.

From the form of the interpolators we construct a correlation function which takes the following form in the continuum limit

$$C_\Gamma(z) = \int_0^\beta dt \int_{-\infty}^{\infty} dy \int_{-\infty}^{\infty} dx \left\langle O_\Gamma(x,y,z,t) O_\Gamma(0,0,0,0)\right\rangle . \tag{4.10}$$

On the lattice the integrations become simple sums over the lattice extents in all but the direction of interest

$$C_\Gamma(z) = T\sum_t^{N_t}\sum_x^{N_x}\sum_y^{N_y} \left\langle O_\Gamma(x,y,z,t) O_\Gamma(0,0,0,0)\right\rangle , \tag{4.11}$$

where O_Γ is the quark interpolator with the γ_μ relabeled as Γ now considered an element of the Clifford algebra.

4.2.1 Flavor Structure and Isospin J=1

In the case of $N_f = 2$ the flavor is exactly described by the generators of $SU(2)$, however, recall that in chapter 2 F^a is a generic element of the set of generators. The set of generators of flavor transformation can be categorized into the flavor singlet F^s and the flavor mixing generators F^n. For the meson correlator the states belonging to the flavor singlet and states belonging to the non-singlet transformations are distinct, and represent both different particle spectra as well as different probes of symmetries.

Putting aside the particle spectrum for a moment, symmetries can be studied a number of ways, one such procedure is to use the condensate operators associated with the singlet and triplet scalar and psuedoscalar channels. While this has been explored in [34], there are some ways in which this analysis does not offer an intuitive understanding in the changing behavior of the mesons with respect to temperature.

For this reason we will consider looking at correlators associated with a single set of flavor transformations, in particular we will focus on the $J = 1$ isospin flavor triplet. The choice to use the isospin triplet is consistent with our desire to look at the channels which are related by symmetry transformations, specifically the channels which are exact chiral partners. For this reason we choose to look at the symmetries directly from the correlators themselves.

This means our quark bilinears are now described by:

$$O^a_\Gamma(x) = \bar{q}(x)(\frac{\tau^a}{2} \otimes \Gamma)q(x). \tag{4.12}$$

In choosing the isospin triplet we may also compare our correlators to the particle spectrum which includes the pion allowing a critical check on the health of our simulations at low temperature.

Moving beyond $N_f = 2$, the $SU(2)$ algebra describing the two degenerate lights quarks has an approximate form of this same symmetry in the case of $N_f = 2 + 1$ and can be split from more complex flavor structure including heavier partners following the same logic. This is well described in the table in [12] along with analogous treatments in [58, 59] and extensions to $N_f = 2 + 1 + 1$ in [25, 26].

4.3 Spatial Correlations

Because we are interested in the symmetries of quarks at finite temperature, and by extension the mesons, we must consider the long range behaviors of the two point correlator with respect to the spatial direction. There is an analogous treatment of the energetic spectrum in the spatial correlator which measures the mass of the energetic region internal to the mesons called the screening mass. Recall the form of the spatial correlator in the z-direction, (4.11). Analogous to the masses which may be extracted from the temporal correlation function at long time extensions, we expect that in the long range of the spatial correlator the screening mass of the meson can be broken into a spectrum

$$C(z) = A_0 e^{-M_0 z} + A_1 e^{-M_1 z} + \dots, \tag{4.13}$$

on a lattice with periodic boundaries we expect that the correlator actually has a second contribution from the far edge near to the source due to our periodic boundary conditions. If we measure from the source to the midpoint of the spatial volume we expect that the spatial correlator(for a sufficiently large spatial volume) has the form

$$C(z) = A_0 e^{-M_0 z} + A_0 e^{-M_0(N_z - z)}, \tag{4.14}$$

around the midpoint we can then make make the approximation of a cosh like function

$$C(z) = A_0 e^{-M_0 N_z/2} \cosh[M_0(z - N_z/2)]. \tag{4.15}$$

To strengthen this approximation we can also fold the form of the correlator around the midpoint as an additional statistical control on fluctuations in the correlator. As the mass should match the meson screening mass around the midpoint we can better assess the long range behaviors using the folded form of the correlator.

There are a few methods to extract the long-range screening mass corresponding the energetic region which makes up the meson, two which we will use are the spatial effective mass which may be determined by simple numerical methods and non-linear least squares fits which may extract the mass term in (4.15).

4.4 Very High T correlation functions

At sufficiently high temperatures the correlation function is solvable through perturbation theory by means of an effective theory of QCD in the non relativistic limit, aptly shortened to NRQCD.

To sketch out NRQCD_3 let us look at the momentum space form of the correlator (4.10),

$$C_{\mathbf{q}} = \int_0^\beta dt \int_{-\infty}^{\infty} \frac{d^3x}{(2\pi)^3} e^{i\mathbf{q}\cdot\mathbf{x}} \langle O_\Gamma^a(\mathbf{x}, t) O_\Gamma^b(\mathbf{0}, 0)\rangle \tag{4.16}$$

In particular we can introduce discretization of the temporal momentum in the Euclidean time direction through the Matsubara frequencies $p_n = 2\pi T(n + \frac{1}{2})$. As the full correlation function contains both fermionic and gauge field terms we will consider the lowest order contribution to the correlator to be fermions in a background field at high temperature. This is motivated by a simple redefinition of the free fermion propagator

$$S(q) = \langle 0|\bar{\psi}(q)\psi(q)|0\rangle\,, \tag{4.17}$$

to include flavor and dirac spinor transformations

$$K^{ab}(q')S(q) = \delta_{ab}\delta(q' - q)f(q^2). \tag{4.18}$$

Where $K^{ab}(q')$ is the associated propagator which contains information from the bilinear operators

$$K^{ab}(q') = \langle 0|\bar{\psi}O_\Gamma^a q'\psi\bar{\psi}O_\Gamma^b(q')\psi|0\rangle\,. \tag{4.19}$$

Meaning that the structure of the free field is simply modified by an algebraic term, and therefore, information about the spatial correlators can be derived from solutions to the free

fermion propagator. Thus the form of the propagator for our momentum space correlation function, in dimensional regularization,

$$C_{\mathbf{q}}[O^a, O^b] = \frac{1}{4}\mathrm{Tr}[\tau^a\tau^b]N_c T \sum_{n=-\infty}^{\infty}\int_{-\infty}^{\infty}\frac{d^{3-2\epsilon}\mathbf{p}}{(2\pi)^{3-2\epsilon}}\frac{\mathrm{Tr}[(\not{p}_n + \not{q})\Gamma^a \not{p}_n \Gamma^b]}{(p_n^2+\mathbf{p}^2)(p_n^2+(\mathbf{p}+\mathbf{q})^2)} \tag{4.20}$$

$\mathbf{p}$ represents the initial momentum of the quarks and $\mathbf{q}$ is the parameter associated with the momentum change from the initial to final vertex point. In particular $\mathbf{q}$ is associated with a momentum spectrum corresponding to the energies of interactions in the short (large q) or long (small q) range.

Following the procedure discussed in the paper by Laine and Vepsäläinen [12], we can do a non-relativistic treatment for the quarks in the energetic regime where the timelike component of the momentum can be treated as a complete "mass" and the correlator can be treated as a 2+1-d theory where the z-direction, the direction of polarization for the correlator, can be treated as a timeike parameter which allows us to determine a spectrum of excitation in the spatial correlators. This treatment of the timelike momentum of the mass is well supported by the explicit dependence on temperature in the Matsubara frequencies; implying that at sufficiently high temperatures even the light quarks are sufficently "massive" to be expressed in a non-relatvistic perturbative framework.

Critically, in [12] the authors show that the lowest order in the expansion of this high temperature correlator is $2\pi T$ the groundstate Matsubara frequency. The result, which is spin independent, indicates that for sufficiently high temperatures the meson masses become degenerate and appear to have a larger symmetry. This symmetry which we will cover later may be the same symmetry studied in previous works [15, 18, 19, 25, 26].

Aside from this the authors of [12], discuss the additional correction to the mass of the meson which is of $\mathcal{O}(g^2T)$

$$M = 2\pi T + Cg^2T + \mathcal{O}(g^4T), \tag{4.21}$$

where C is a numerical constant derived from numerical solutions of the Bethe-Salpeter approach to the "groundstate" of the correlator.

For $N_f = 2$ QCD on the lattice at very high temperatures we may be able to verify this correction from below as we are both interested in these high temperature corrections while also looking for signals of symmetry restoration. From the very high temperature analysis of the correlators we know that the spin independent corrections ($\mathcal{O}(g^2T)$ terms) to the screening mass has some evidence, demonstrated at $T > 1$GeV in [1] by Dalla Brida et al. However, indications of this correction from below are difficult to detect as this quantity requires a theoretically clean approach to the screening mass to detect any possible effects from the coupling at lower temperatures. Previous work looking for evidence of the leading order contribution to to the screening mass found it difficult to detect from below the chiral transition point [2] and stated that $T \sim 1$GeV were insufficient to capture the corrections.

Chapter 5

Mesonic Two-Point function and Symmetries at High Temperature

As discussed in chapter 2, QCD is exactly invariant under $SU(2)_L \times SU(2)_R$ in the massless limit as well as the axial symmetry transformation $U(1)_A$. However, it is well known that the symmetry $U(1)_A$ is, in general, broken by the axial anomaly which for finite temperatures is strongly connected to the topological gluon fluctuations. There is evidence that at high temperatures the topological gluon excitations are actually suppressed and we have effective "restoration" of $U(1)_A$. More recently, the question of interest is not whether the restoration of $U(1)_A$ occurs but at what temperature as this impacts the nature of the chiral phase transition.

5.1 The two-point correlator and probes for chiral symmetry

Due to the symmetry in the two point correlation function expressed in (5.3) and (5.4) we can look at a number of different quantities to study the behavior of the lattice with respect to temperature. Such quantities, which are ultimately connected to the correlation functions, have their respective theoretical motivations and together give us a robust description of the chiral crossover and high temperature lattice. Previous work has studied two quantities of interest chiral susceptibilities and the proportions of correlation functions.

In the works [13, 15, 25, 26], the authors looked at chiral symmetry and the chiral spin using a ratio between the differences of the correlation functions directly. The proportion of the correlators has the advantage of being straightforward to analyze, however, this is subject to noise in the far range of the correlators; in channels with larger screening masses the correlators rapidly tend toward zero making proportions very sensitive to noise in several of the channels.

Work by [34], and JLQCD [4, 5, 6, 7, 24, 30, 33] studied chiral symmetry from the susceptibilities by way of the chiral condensate. The susceptibilities by themselves are quite a good quantity to study, and can be related to the two point correlation function by integration of both the spatial and temporal directions. Their connection to the chiral symmetries requires some additional motivation but is quite straightforward for the $SU(2)_L \times SU(2)_R$ symmetry.

The $U(1)_A$ sector has been shown to connect to the topological susceptibility and does appear to connect to the $SU(2)_L \times SU(2)_R$ sector by way of the connected susceptibility from eigenvalue decomposition of the Overlap operator. Analysis of the axial $U(1)$ susceptibility does require calculation of the disconnected susceptibility, which also requires calculations of the topological susceptibility

$$\chi_A^{dis}(m) = \frac{2}{m^2 V} \langle Q^2 \rangle . \tag{5.1}$$

5.1.1 Effective Mass and Screening Mass

In addition to these two previously studied quantities we can also study temperature, mass dependence and chiral symmetry from the two point correlation function using an additional quantity: the spatial screening mass. The screening mass is a quantity which can be extracted from the correlation function by way of fit to the hyperbolic cosine ansatz from section 4.3.

The spatial screening mass is an analogous quantity to the mass which can be extracted from the temporal correlation function. In the case of the screening mass we are not interested in analyzing the spectrum of masses as this quantity can be used, like the other quantities derived from the correlation function, to probe changes in the meson symmetries. To extract the long range screening mass we need a method to check when we have reached the long range "groundstate" mass. To determine this first we use the effective mass of the correlators to extract the effective mass at each position using the neighboring site

$$\frac{C(z+1)}{C(z)} = \frac{\cosh[M_0(z+1-N_z/2)]}{\cosh[M_0(z-N_z/2)]}. \tag{5.2}$$

Using any numerical method we can use this proportion to extract both the mass and amplitude as a function of z/a. Due to the proportion of correlators, this quantity is subject to massive fluctuations, in particular, whenever the correlator is very close to zero the effective mass becomes unreliable due to extreme sensitivity to the small fluctuations in the correlator near zero. In fig. 5.1(a) all six correlator channels are plotted for the lowest temperature in the $N_f = 2$ study. The folded correlators for S, A_x and X_t either drop to zero or negative for $z/a = 8$, $z/a = 15$ and $z/a = 12$ respectively; from the effective mass curves fig. 5.1(b), 5.1(e), and 5.1(g) we can see that this drop in value for the correlator typically coincides with a massive increase in instability of the effective mass[1].

5.2 Symmetries of the two-point correlator

To this end in looking at symmetries of QCD from the lattice we will use a quantity derived from the spatial mesonic two point correlation function in z which has the following form in the continuum,

$$C_\Gamma(z) = \int_0^\beta dt \int_{-\infty}^{\infty} dx \int_{-\infty}^{\infty} dy \, \langle O_\Gamma^a(x,y,z,t) O_\Gamma^b(0,0,0,0) \rangle \, \delta^{ab}. \tag{5.3}$$

[1]In some cases such as fig. 5.1(b) the fluctuations are so severe that Gnuplot will not plot the central values and errors as the value(when not NaN due to overflow errors) is far outside the plot range.

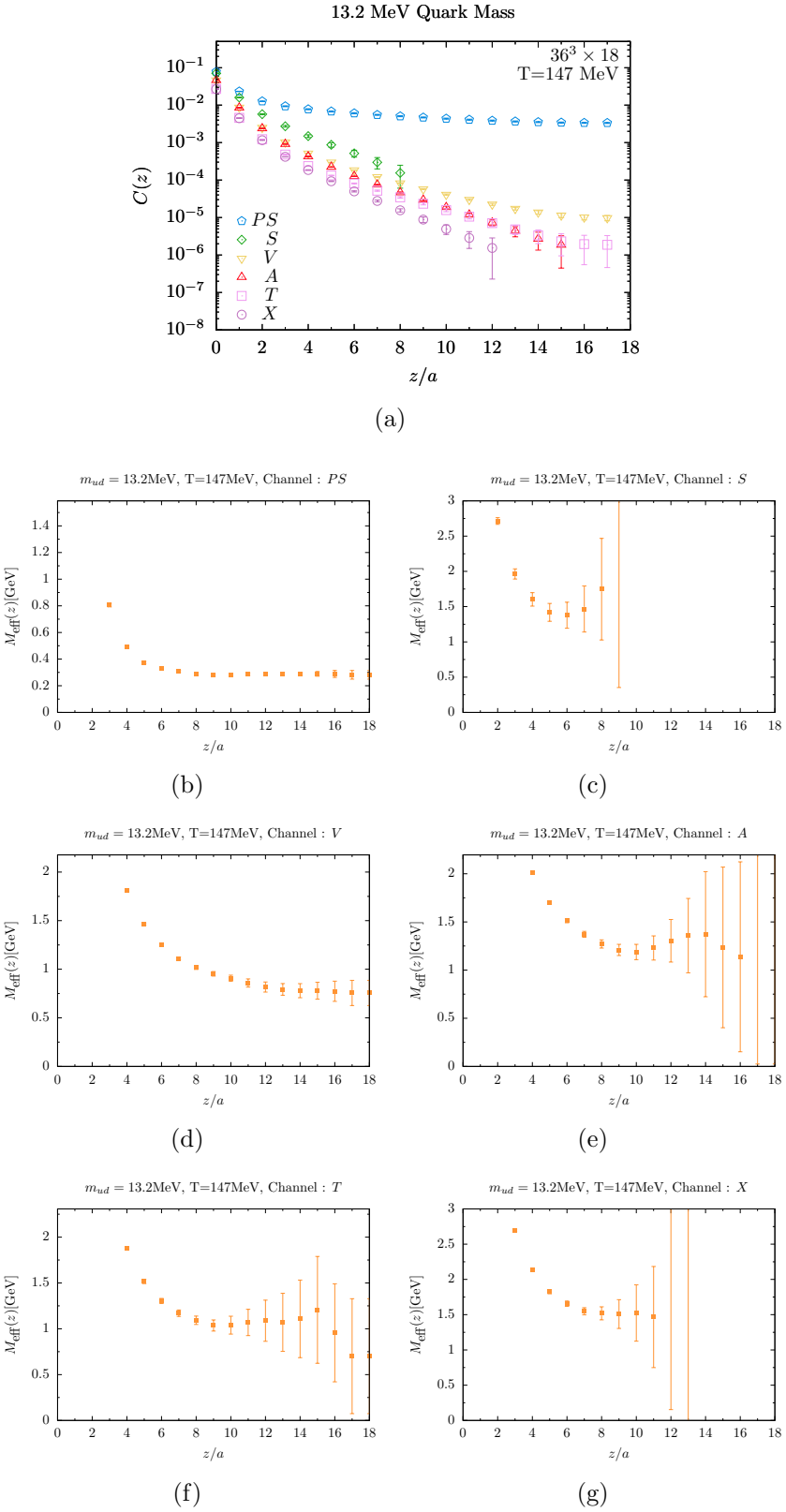

Figure 5.1: An example of $am = 0.0050$ correlators at $T = 146$MeV using the 36×18 ensemble along with the behavior of the associated effective masses.

This quantity takes on a similar form to (4.11) on the lattice and is simply the form of (4.10) which measures correlations for spatial separations. As such the form of the quark bilinear is the same as the form of the isospin bilinear operator from 4.2.1:

$$O^a_\Gamma = \bar{q}\left(\Gamma \otimes \frac{\tau^a}{2}\right)q. \tag{5.4}$$

The correlator has six channels consistent with the choices of Γ written in equations (4.4)-(4.9) and summarized(along with their symmetry multiplets) in 5.1.

In chapter 2 we considered a generic chiral symmetry in the lagrangian, in the case of the interpolator and correlations function only certain channels remain invariant while other channels will mix under symmetry transformations. Thus under the standard $SU(2)_L \times SU(2)_R$ symmetry

$$\bar{q} \rightarrow \bar{q}e^{i(\tau^a\gamma_5\theta^a - \tau^b\phi^b)}, \tag{5.5}$$
$$q \rightarrow e^{i(\tau^a\gamma_5\theta^a + \tau^b\phi^b)}q, \tag{5.6}$$

only the vector like V and A channels of the correlator mix while the PS, S and tensor channels all remain invariant. Therefore, the difference between the V and A correlators serves as a probe of the $SU(2)_L \times SU(2)_R$ symmetry.

Likewise the axial $U(1)_A$ transformation,

$$\bar{q} \rightarrow \bar{q}e^{i\gamma_5\alpha}, \tag{5.7}$$
$$q \rightarrow e^{i\gamma_5\alpha}q, \tag{5.8}$$

mix the PS and S channels as well as the tensor X_t and T_t channels respectively while the vector channels V and A of the correlator remain invariant. This indicates that we actually have two probes for $U(1)_A$ the $S-PS$ and T_t-X_t differences; this redundancy is actually to our benefit as S the channel is quite noisy for low temperatures (see figs. 5.1(a) and 5.1(b) as well as the next chapter), therefore having the $T_t - X_t$ pair offers us a more reliable probe which can be used alongside the $S - PS$ difference.

Γ	Reference Name	Abbr.	Symmetry Correspondences	
$\mathbb{1}$	Scalar	S	$U(1)_A$	
γ_5	Psuedo Scalar	PS		
γ_1, γ_2	Vector	V	$SU(2)_L \times SU(2)_R$	$SU(2)_{CS}$
$\gamma_1\gamma_5, \gamma_2\gamma_5$	Axial Vector	A		
$\gamma_0\gamma_3$	Tensor	T_t	$U(1)_A$	
$\gamma_0\gamma_3\gamma_5$	Axial Tensor	X_t		

Table 5.1: List of quark bilinear operators we compute the two-point correlation functions and the symmetries connecting them.

There is, in addition, to the previously described symmetries of the QCD Lagrangian an emergent set of symmetries which may indicate a larger symmetry structure at high temperatures. These potential larger effective symmetries are connected to the anti-periodic

boundary condition on the quarks in the temporal direction due to the compactification for finite temperatures. This emergent symmetry is analogous to the heavy quark symmetry [21, 20], an approximate symmetry which appears in the effective theory for charm and bottom quarks. To examine this symmetry let us consider the form of the free quark propagator with momenta p_1, p_2 perpendicular to the z-axis

$$\begin{aligned}\langle q(z)\bar{q}(0)\rangle\,(p_1,p_2) &= T\sum_{p_0}\int\frac{dp_3}{(2\pi)}\frac{e^{ip_3 z}}{i\gamma_0 p_0+i\gamma_3 p_3+i\gamma_1 p_1+i\gamma_2 p_2+m},\\ &= T\sum_{p_0}\int\frac{dp_3}{(2\pi)}\frac{-(i\gamma_0 p_0+i\gamma_3 p_3+i\gamma_1 p_1+i\gamma_2 p_2-m)e^{ip_3 z}}{p_0^2+p_3^2+p_2^2+p_1^2+m^2}.\end{aligned}$$

The perpendicular momenta can be treated as fixed parameters and thus the integration along z has a pole at $-ip_3 = E(p_0, p_1, p_2)$ where

$$E(p_0,p_1,p_2)=\sqrt{p_0^2+p_1^2+p_2^2+m^2}. \tag{5.9}$$

The temporal component of the momentum is already parameterized and takes on discrete values consistent with the description by the Matsubara mass

$$p_0=(n+1/2)2\pi T, \tag{5.10}$$

which comes from the antiperiodic condition in the temporal direction. Using these properties the propagator takes on the form

$$\langle q(z)\bar{q}(0)\rangle\,(p_1,p_2)=T\sum_{p_0}\frac{-(i\gamma_0 p_0-\gamma_3 E+i\gamma_1 p_1+i\gamma_2 p_2-m)}{2E(p_0,p_1,p_2)}e^{-Ez}. \tag{5.11}$$

At large separations and high temperatures the lowest Matsubara frequency dominates with $p_0 = \pm\pi T$; in particular we will consider taking the $T \to \infty$ limit, which is sufficient to satisfy the condition $T \gg p_1, p_2, m$, where the lowest mass saturates the "energy" (5.9) allowing us to expand in powers of $1/T$:

$$\langle q(z)\bar{q}(0)\rangle\,(p_1,p_2)=T\left[\gamma_3\frac{1+i\mathrm{sgn}(p_0)\gamma_0\gamma_3}{2}e^{-\pi Tz}+\mathcal{O}(1/T)\right]. \tag{5.12}$$

This high temperature expansion is not unique and can also be done for p_0 with fixed spatial momentum $\mathbf{p}$, the analogous term for the temporal correlation function is

$$\langle q(t)\bar{q}(0)\rangle\,(p_1,p_2,p_3)=-iT\left[\sum_{p_0}\frac{\gamma_0 p_0}{p_0^2}e^{-ip_0 t}+\mathcal{O}(1/T)\right]. \tag{5.13}$$

Both of these propagators transform invariantly under an effective $SU(2)$ vectorlike symmetry:

$$q \to e^{i\Sigma^i\xi_i}q, \tag{5.14}$$

$$\bar{q} \to \bar{q}\gamma_0 e^{-i\Sigma^i\xi_i}\gamma_0. \tag{5.15}$$

Where Σ^i has three components,

$$\Sigma^i = \begin{bmatrix} \gamma^k \\ -i\gamma_5\gamma^k \\ \gamma_5 \end{bmatrix}, \quad k = 1, 2. \tag{5.16}$$

Due to rotational invariance around the z-axis, the $k = 1$ and $k = 2$ components are identical and so will be generically described using k. This $SU(2)$ algebra is identified with the chiral-spin $SU(2)_{CS}$ symmetry suggested in [16, 17, 18, 19, 61, 62].

While we have considered a free quark propagator, in QCD the gauge field contributions to the propagator appear at next-to-leading order in the $\mathcal{O}(1/T)$ term. Therefore, at sufficiently high temperatures the $SU(2)_{CS}$ is an emergent symmetry for which we can find the appropriate symmetry multiplet. Previous work identifying multiplets [15, 25, 26], has shown that a triplet (A_x, T_t, X_t)[2] of mesonic correlators transforms consistent with (5.14) and (5.15). For the $SU(2)_{CS}$ symmetry we an construct several multiplets which would appear to transform under this isospin symmetry such as (V_y, PS, S). However, due to our choice to fix the correlator around the z-axis these states, which have different spins in the original four dimensions, now transform under the spin-one representation of $SO(3)$. Due to this additional rotational symmetry, we can distinguish various multiplets based on their mass degeneracy associated iwth this rotation; in the case of the (V_y, PS, S) multiplet we find that while these do transform under $SO(3)$ V_y and PS, S transform differently under $SO(3)$ resulting in a weaker mass degeneracy. In the case of (A_x, T_t, X_t) all three channel transform into one another in the same vector-like representation resulting in a triplet for which the masses of the channels are degenerate.

Consistent with our discussion of the perturbative results from NRQCD in chapter 4 we find that our free quark propagator in the high temperature limit is consistent with the expected meson screening mass result of $2\pi T$ in the free quark limit. Recall from 4.4 the form of the result from [12]

$$M = 2\pi T + Cg^2 T. \tag{5.17}$$

The next-to-leading order term is simply a one loop correction and like the leading order term both are independent of choice in Γ. This and our effective high temperature form of the free quark propagator show remarkable correspondence in producing a spin independent correction. This behavior is analogous to the approximate heavy quark symmetry at $T = 0$, because this symmetry for heavy quarkonia, as well as, heavy-light mesons shows a similar insensitivity to spin; the reason for this is that spin and angular momentum terms are inversely proportional to the quark mass. In the high temperature limit the ground-state Matsubara mass proportional to T is quite large and operators such as (V_x, PS, S) or (A_x, T_t, X_T) form $SU(2)_{CS}$ triplets.

In [15] the threshold for $SU(2)_{CS}$ emergence was estimated at $T \sim 1.8T_c$, while [17, 16] estimate temperatures between $2T_c - 3T_c$. Using the screening mass difference approach it is important to quantify the emergent behavior of $SU(2)_{CS}$ in the range of temperatures $T_c - 2T_c$ and to determine if there is any impact on the chiral phase transition. In addition to this we would also like to quantify the behavior of the $SU(2)_L \times SU(2)_R$ and $U(1)_A$

[2]There is a partner multiplet (V_x, T_t, X_t) which is simply the $SU(2)_L \times SU(2)_R$ chiral partner and does not constitute a unique triplet.

symmetries in the region from just below the chiral crossover into the high temperature $2T_c$ region to both understand the relationship between these two symmetries in the region of the phase transition as well as assess their high temperature limits. Therefore, we have sufficient motivation to study QCD in range of temperatures $[0.9, 2.0]T_c$ for a range of masses including the physical point as a way to understand the symmetry structure of QCD at high temperatures.

Chapter 6

Symmetries around T_c

6.1 Lattice Setup and Parameters

6.1.1 Lattice configurations

In studying the symmetries there are two distinct and separate numerical caluclations involved, the first step is generation of the configurations; we generated configurations using the Grid software [63], simulations of the lattice were done using hybrid Monte Carlo with the Möbius Domain Wall fermion action [54, 55] and the tree level improved Symanzik improved gauge action. The simulations were done for a fixed bare coupling $\beta = 4.30$ and fixed lattice spacing of $a = 0.0075fm$ [64, 65, 66]. In addition to the new configurations generated for lower temperatures and various volumes, a few of the higher temperature configurations used in previous studies [5, 24] were reused. All of the relevant lattice parameters for our configurations are listed in Tab. 6.1.

Scale setting of the lattice was done by performing a Wilson flow using the reference flow time $t_0 = (0.1539fm)^2$ in [67] to determine a lattice cutoff factor of $a^{-1} = 2.463GeV$. For the ensembles above the lowest temperature, a lattice spatial extent of $L = 32$ corresponding to $2.37fm$ was primarily used. At the lower two temperatures we also measured additional volumes of $L = 48$ and $L = 40$ to study the finite volume systematics at and below the critical temperature.

Because we consider finite temperature lattices with fixed coupling/lattice spacing we varied temperature by changing the temporal extent of the lattices from 18 to 8 in steps of 2, corresponding to the range of temperatures 147MeV $\leq T \leq$ 330MeV or $0.9T_c \leq T \leq 2T_c$. Where the value for the critical at the physical point $T_c \sim 165(3)$MeV is estimated from the peak of the disconnected susceptibility in [6], the uncertainty in the value of the critical temperature is purely statistical.

For the full study we included the new and old configurations which used a variable range of masses depending on the temperature; the bulk of our analysis focused on 4 masses, the lightest of which $am = 0.0010$ corresponds to 2.6MeV, which is estimated to be 71% of the physical quark mass $am_{phys} = 0.0014(2)$. While the target physics is the physical point as part of a potential line of constant physics, the higher mass quarks are included in the study to both study and assess errors in the symmetries of the lightest mass quarks, as well as to understand how the symmetries and critical temperature may change with respect to the

$L^3 \times L_t$	L(fm)	T[MeV]	TL	am	m[MeV]	# samples
$48^3 \times 18$	3.6	147	2.7	0.00100	2.6	146
				0.00250	6.6	40
				0.00375	9.9	40
				0.00500	13.2	83
$36^3 \times 18$	2.7	147	2.0	0.00100	2.6	146
				0.00250	6.6	121
				0.00375	9.9	122
				0.00500	13.2	131
$40^3 \times 16$	3.0	165	2.5	0.00100	2.6	165
				0.00250	6.6	95
				0.00375	9.9	97
				0.00500	13.2	95
$32^3 \times 16$	2.4	165	2.0	0.00100	2.6	165
				0.00250	6.6	116
				0.00375	9.9	163
				0.00500	13.2	143
$32^3 \times 14$	2.4	189	2.3	0.00100	2.6	190
				0.00250	6.6	177
				0.00375	9.9	137
				0.00500	13.2	133
$48^3 \times 12$	3.6	220	4.0	0.00100	2.6	220
				0.00250	6.6	97
				0.00375	9.9	114
				0.00500	13.2	116
$40^3 \times 12$	3.0	220	3.3	0.00500	13.2	220
				0.01000	26.4	244
$32^3 \times 12$	2.4	220	2.7	0.00100	2.6	532
				0.00250	6.6	534
				0.00375	9.9	689
				0.00500	13.2	544
				0.01000	26.4	622
$24^3 \times 12$	1.8	220	2.0	0.00100	2.6	373
				0.00250	6.6	361
				0.00375	9.9	331
				0.00500	13.2	363
				0.01000	26.4	365
$32^3 \times 10$	2.4	264	3.2	0.00500	13.2	640
				0.00800	21.1	237
				0.01000	26.4	291
				0.01500	39.6	121
$32^3 \times 8$	2.4	330	4.0	0.00100	2.6	260
				0.00500	13.2	317
				0.01000	26.4	350
				0.01500	39.6	306
				0.02000	52.9	218
				0.04000	105.7	164

Table 6.1: All lattice ensembles used in the $N_f = 2$ study for finite temperature, the number of configurations are also listed. All lattices use the same $L_s = 16$.

variation in the quark mass.

6.1.2 Configuration Measurement

The second step in our study following configuration generation is extraction of the relevant correlators by inversion of the Möbius Domain wall fermion effective overlap operator from chapter 3, equation (3.78)

$$D_{ov} = \frac{1+m}{2} + \frac{1-m}{2}\gamma_5 \tanh[L_s \tanh^{-1}(H_W)]. \tag{6.1}$$

For the $N_f = 2$ lattice configurations all of the lattices have a Möbius domain wall fermion operator with a length in the fifth dimension of $L_s = 16$. Correspondingly the residual mass, a measure of the chiral symmetry breaking in the Dirac operator, is suppressed to 0.14(6)MeV.

As configurations of the lattice were saved every 10 steps during the simulation, we chose to measure every fifth configuration(every 50th trajectory) to reduce autocorrelation. The result of this is between 40-700 measurements listed in the sample number column of Table 6.1. These lattice configurations were measured first using the IroIro++ package[65], and later using Bridge++ [64] based on speed up and improvements in accuracy. For both measurement softwares we applied a stout smearing [68] three times with the smoothing parameter $\rho = 0.1$. In addition to this we did apply any source smearing, and considered point-like source and sink operators.

6.1.3 Effective Mass and Extraction of Screening masses

Following measurements done by IroIro and Bridge, to obtain the screening masses from the correlation functions we first generated a spatial effective mass by applying Newton's Method to the cosh ansatz form of the spatial correlator (4.15) using the proportion (5.2) of neighboring sites.

As the effective mass alone is not a reliable quantity to determine the screening mass, we employ an additional check by performing an uncorrelated nonlinear least squares fit to the correlator using the same ansatz (4.15). The fit is restricted to the stable range of the correlator and overlaid with the effective mass to compare the value of the fit to the behaviors of the effective mass throughout the fit range. Stability in the correlator curve was indicated by a combination of noise and stability of the central value point by point, the converse to this, an unstable region in the correlator is indicated by either a sign flip in or rapid drop to zero. If the central value of the fit is within 2σ for the effective mass values in the range and the effective mass appears to plateau, then the fit is considered accurate and we can trust that we have extracted the screening mass for the meson from the correlator.

For regions in which the correlator is stable we extracted screening masses for each of of six channels. For the set of chiral symmetries $SU(2)_L \times SU(2)_R$ and $U(1)_A$, we fit both channels of the symmetry multiplet $V - A$, $PS - S$ and $X_t - T_t$ to the same range. As an additional check on the screening mass behaviors we also performed several fits to verify that our reported screening masses did not significantly depend on a narrow fitting range and the systematic errors were well controlled compared with error from the statistical uncertainty.

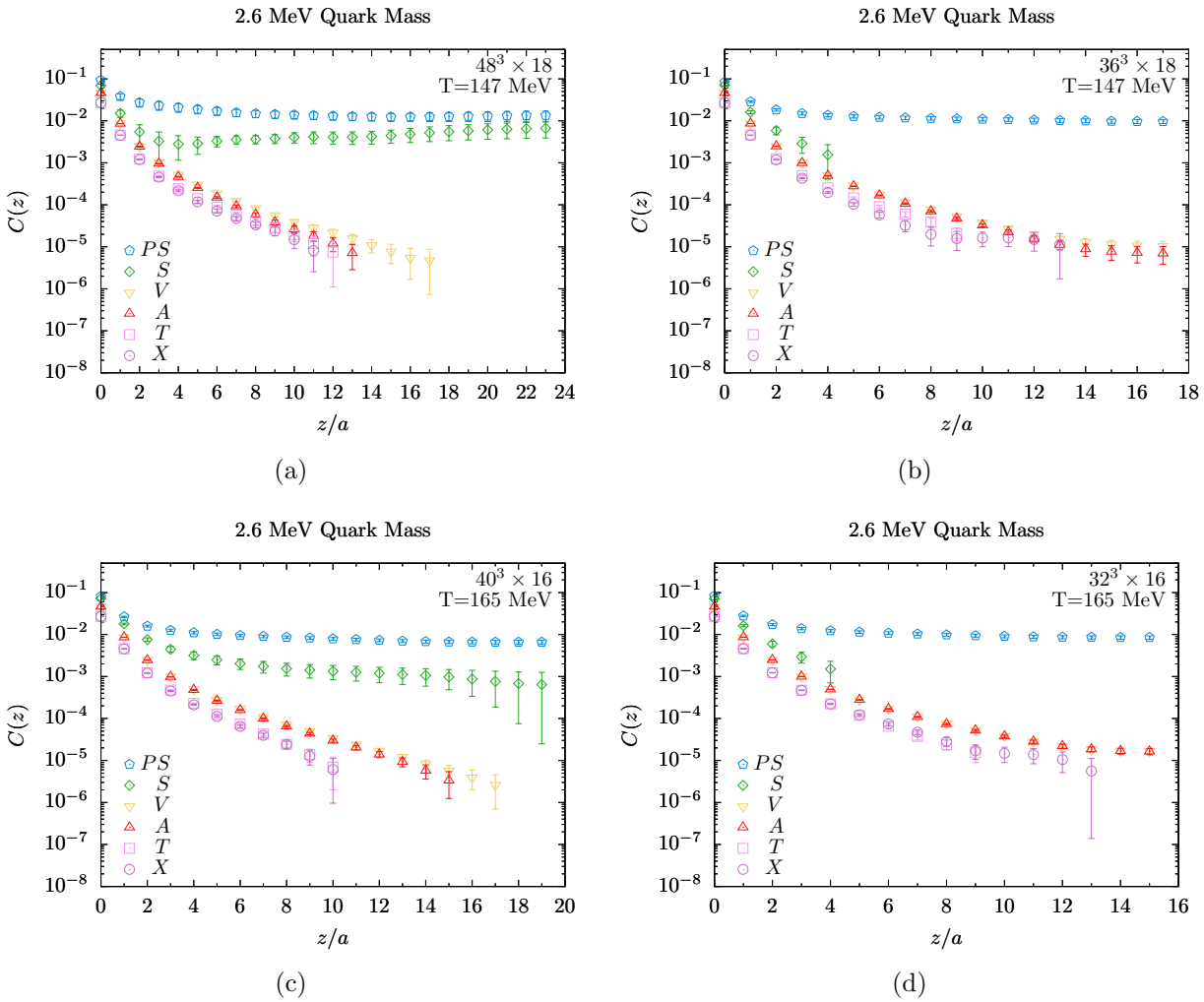

Figure 6.1: These are correlator plots for the two lowest temperatures in $N_f = 2$ QCD from the lightest quark mass ensembles.

6.2 Numerical Results

In the course of analysis, the S channel correlator was found to be quite unstable, this instability reflects exceptional spikes in the thermal history from only a handful of configurations; this problem is especially acute for the correlators measured on low temperature figures 6.1(a) and 6.1(b) are two examples of very noisy S channel behaviors. Consistent with our fitting procedure from 6.1.3 the S channel values were omitted when the screening mass flipped sign or could not be fit to a stable plateau for the same range as the PS channel.

Figures 6.3, 6.4, and 6.5 show the the effective mass curves with the screening mass fits overlaid for the three lowest temperatures for the lighest quark mass $am = 0.0010$. In addition to these plots we also have the Table 6.2 summarizing all of the extracted screening masses for all lattices and masses in this study. To show the core behaviors around the physical point only the lightest mass fits fits are shown.

In addition to the lower temperature plots we also have Figs. 6.6 and 6.7 for the physical

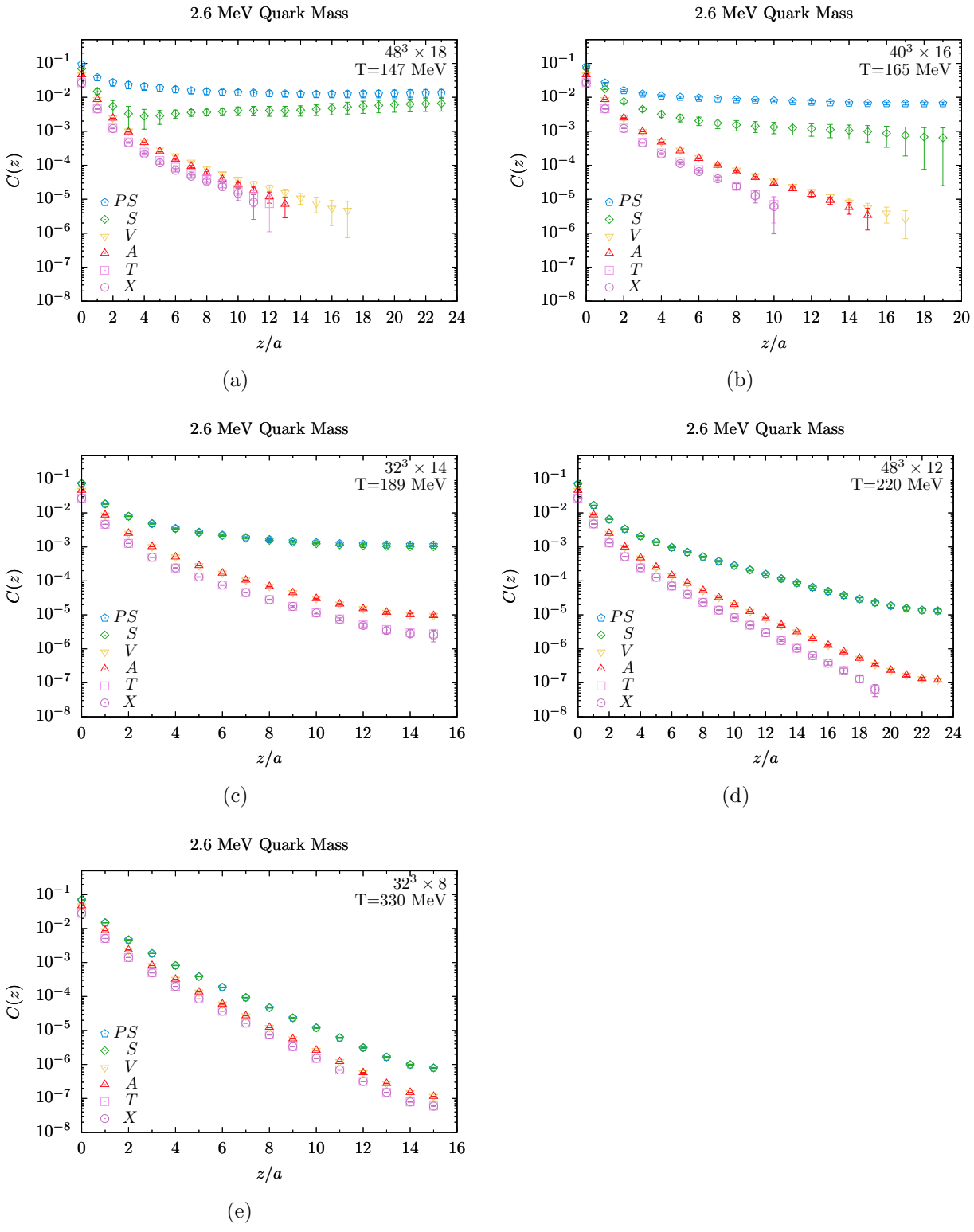

Figure 6.2: These are correlator plots for the range of temperatures in $N_f = 2$ QCD from the lightest quark mass ensembles.

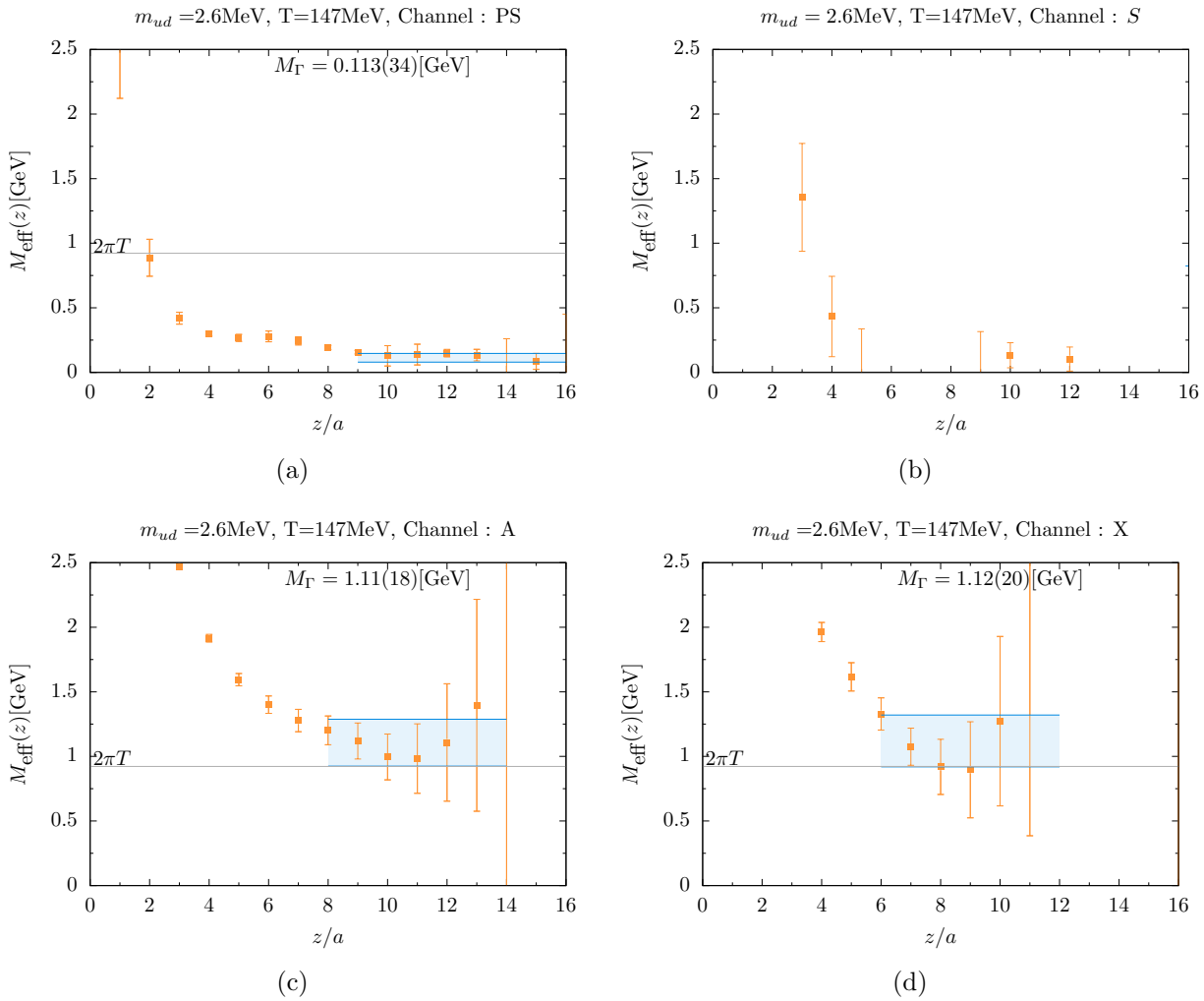

Figure 6.3: Fits compared with the effective screening mass from the $T = 147$MeV correlation function in 6.2(a).

point mass. the $32^3 \times 10$ lattice corresponding to the temperature corresponding to $T = 264$MeV, did not include masses around the physical point and is included in analysis of the symmetries for the $am = 0.0050$ lattices. Plots of the temperature dependence which are shown for the lightest masses are included in the appendix.

For this study using the Möbius Domain wall fermions despite noise at low temperatures seen in the correlators in figure 6.1 or figure 6.2, we have no problems determining the plateaus of the effective mass during fit. This is in contrast to the the work done by HotQCD in [2], where the authors reported a significant contamination of the groundstate plateaus by excited states. The reason for this difference in determining a groundstate plateau in the effective mass may be due to the fact that the Möbius domain wall fermions are theoretically clean and do not encounter any operator mixing from the multiplets of the $SU(2)_L \times SU(2)_R$ symmetry group; this is in addition to avoiding unphysical excitations which are introduced by the taste degrees of freedom.

Figures 6.3-6.7 show the fit ranges and fit bands for which we extracted the screening

masses presented in Tables 6.2 and 6.3. In the fit plots we show only have of the partner pair for the symmetry multiplet as the fit ranges were determined by cross comparison of the fit for the same range across both partners in the symmetry multiplet. In contrast to this the S channel is shown to illustrate the noise present in fitting the correlator for all temperatures in this study. In addition to this all plots shown are restricted $z/a = [0, 16]$ and $M_{eff} = [0, 2.5]$GeV to allow direct comparisons of the screening mass and Matsubara frequencies for all lattices.

6.2.1 Thermal dependence of the meson screening mass

Using the extracted screening masses, we plotted the temperature dependence of the meson screening masses for all quark mass ensembles. Figure 6.8, shows the temperature dependence of the screening mass for the lightest quark $am = 0.0010(2.6\text{MeV})$. As mentioned before in chapters 5 and 4 in the high temperature limit all of the channels appear to converge

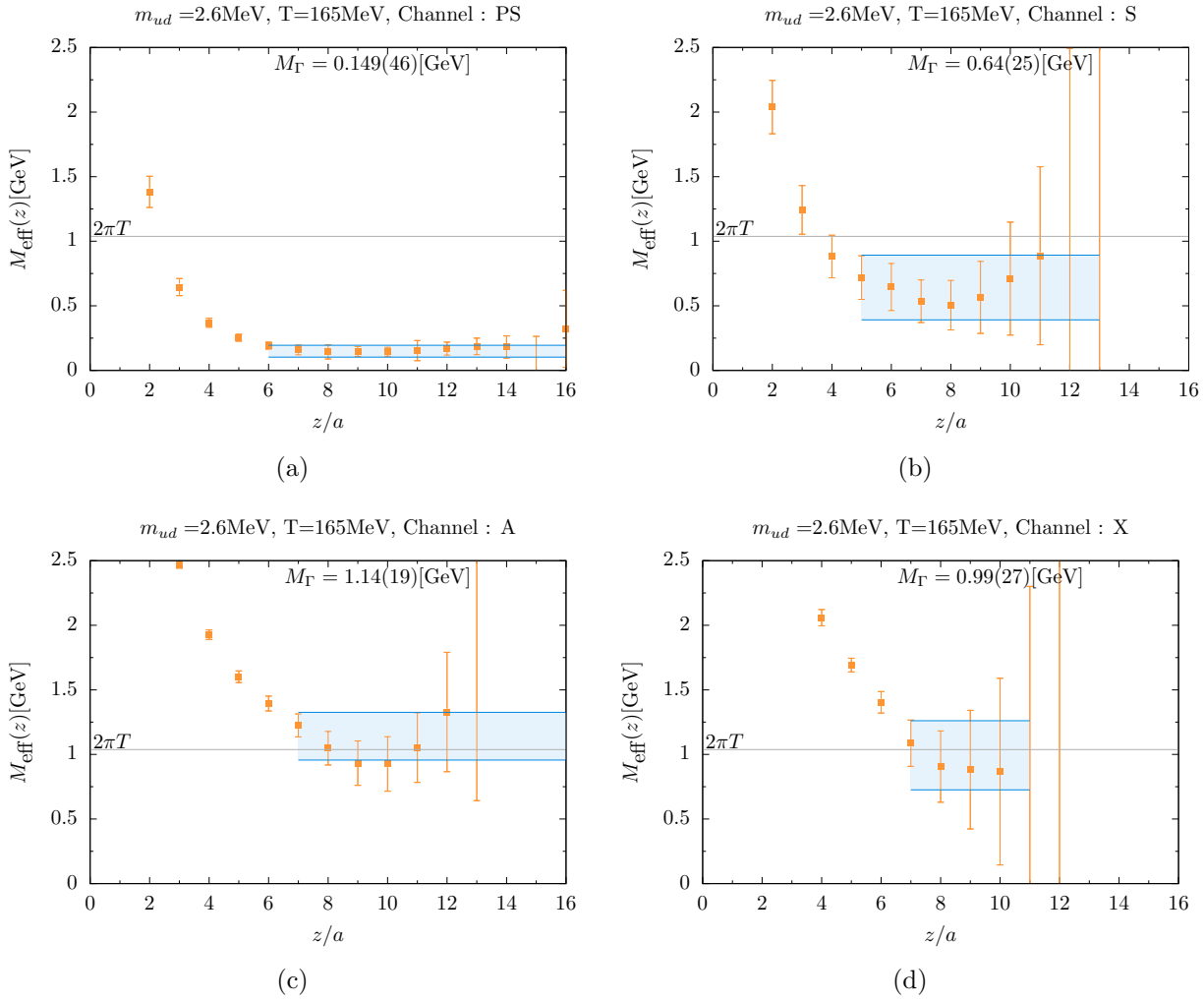

Figure 6.4: Fits compared with the effective screening mass from the $T = 165$MeV correlation function in 6.2(b).

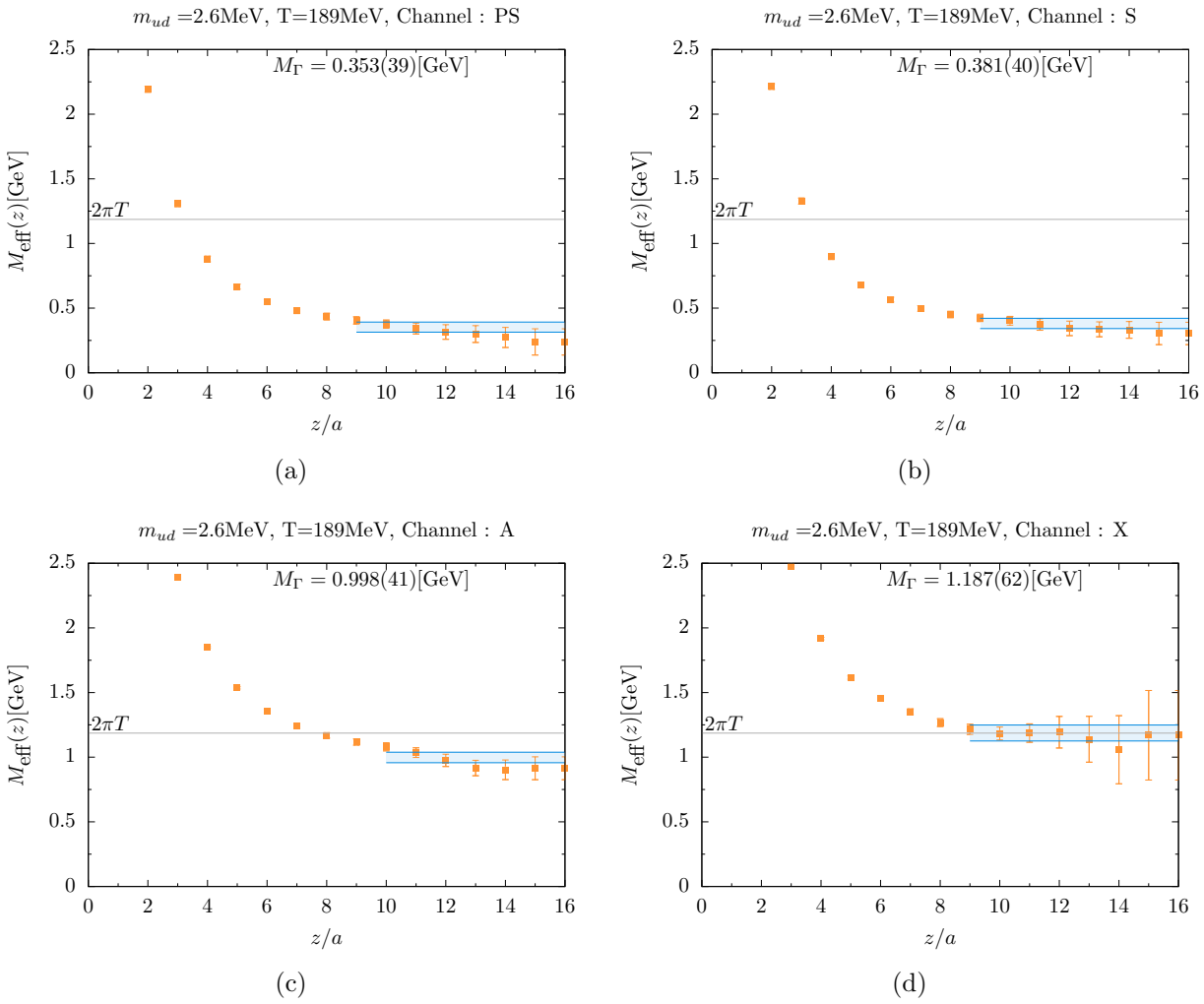

Figure 6.5: Fits compared with the effective screening mass from the $T = 189$MeV correlation function in 6.2(c).

to $2\pi T$, twice the groundstate Matsubara mass, plotted as a solid grey line. In particular, the heaviest channels X_t and T_t very rapidly converge to $2\pi T$ almost immediately following the chiral phase transition, shown as a vertical grey band. At temperatures around or below the critical temperature $T_c \sim 165(3)$MeV, the aforementioned verical grey band, there is a dramatic shift in the fluctuation of the screening mass which appears highly reduced above the line of chiral phase transition. The Scalar channel screening mass, in particular, shows significant fluctuation at T_c after which the screening mass rapidly converges to a value near the Pseudoscalar channel for all higher temperatures.

At low temperatures $T = 0$ experimental values are plotted as reference lines for the $J = 1$ meson spectrum, $\pi^\pm$, ρ, a_0, and a_1. These are color coded in correspondence with their associated meson interpolators channels. At $0.9T_c$ it is interesting to note that for $N_f = 2$ the screening mass already show significant overlap with the $T = 0$ experimental results; this indicates that chiral symmetry breaking through the chiral condensate is already sufficiently large to form hadrons. In the $T = 0$ limit due to the susceptibility to the $U(1)_A$

anomaly, X_t and T_t transform similar to the vector channels A and V resulting in overlapping intermediate states.

In [2], the authors studied $N_f = 2+1$ QCD at a range of temperatures from below T_c up to approximately 1GeV using HISQ fermions. To make an effective comparison between their extrapolation to the continuum theory and our results in Fig. 6.9 we normalized the screening mass by $2\pi T$ and normalized the temperature by T_c, for $N_f = 2$ this is $T_c \sim 165$MeV and for $N_f = 2+1$ we used the estimated temperature of $T_c \sim 156$MeV from [2]. While the critical temperatures do differ due to the presence of the strange quark in the $N_f = 2+1$ results, when normalized both curves show a remarkable consistency in the characteristics of the curves at all temperatures. The key difference between our study an that of the $N_f = 2+1$ study by HotQCD is the S channel, for the HISQ fermions there is a well known lattice artifact which allows the S channel meson to decay to two pions and so at $T = 0$ the HISQ fermions approach $2\pi^{\pm}$(shown as a green shadown in 6.9). In contrast to this, the artifact

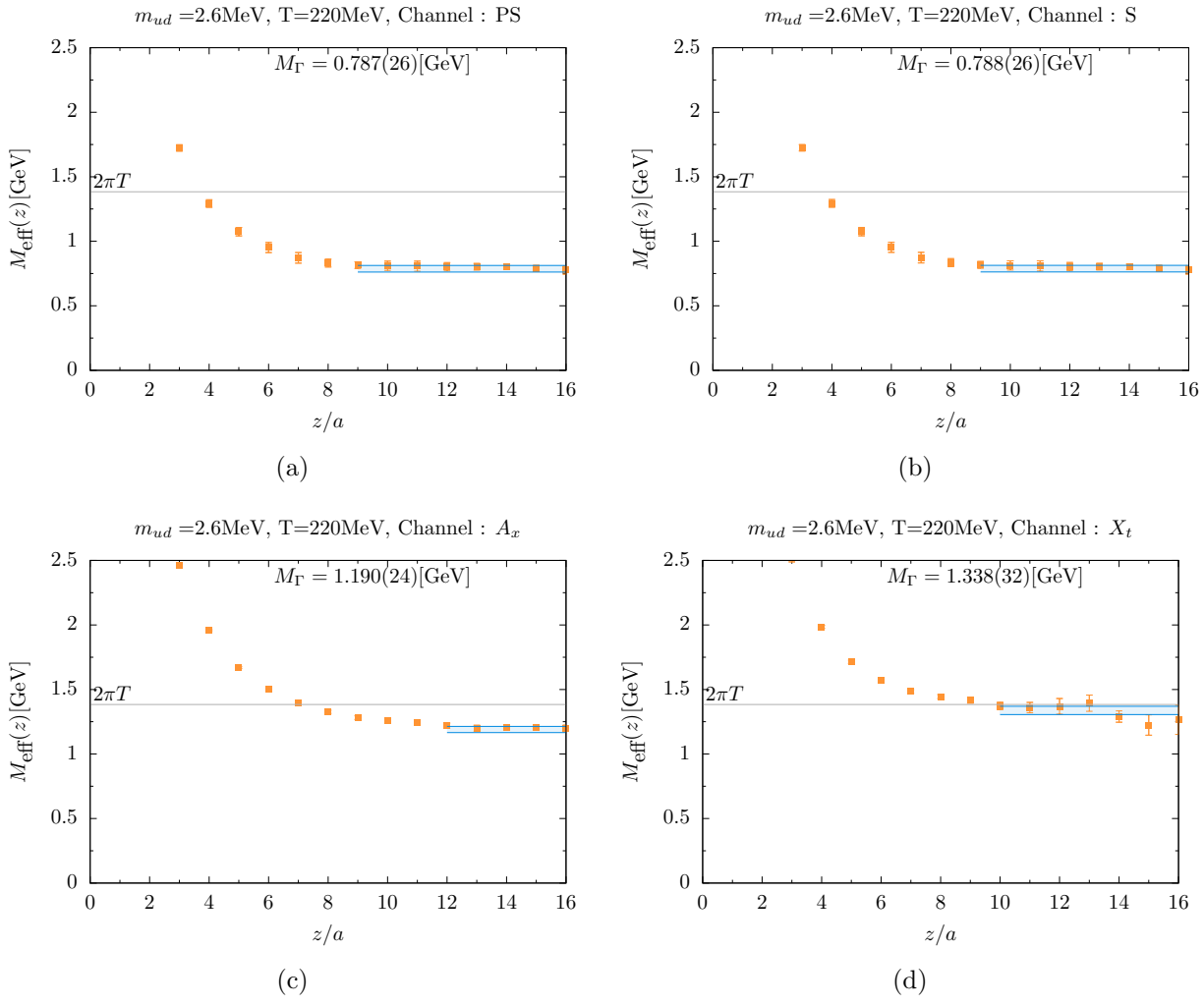

Figure 6.6: Fits compared with the effective screening mass from the $T = 220$MeV correlation function in 6.2(d).

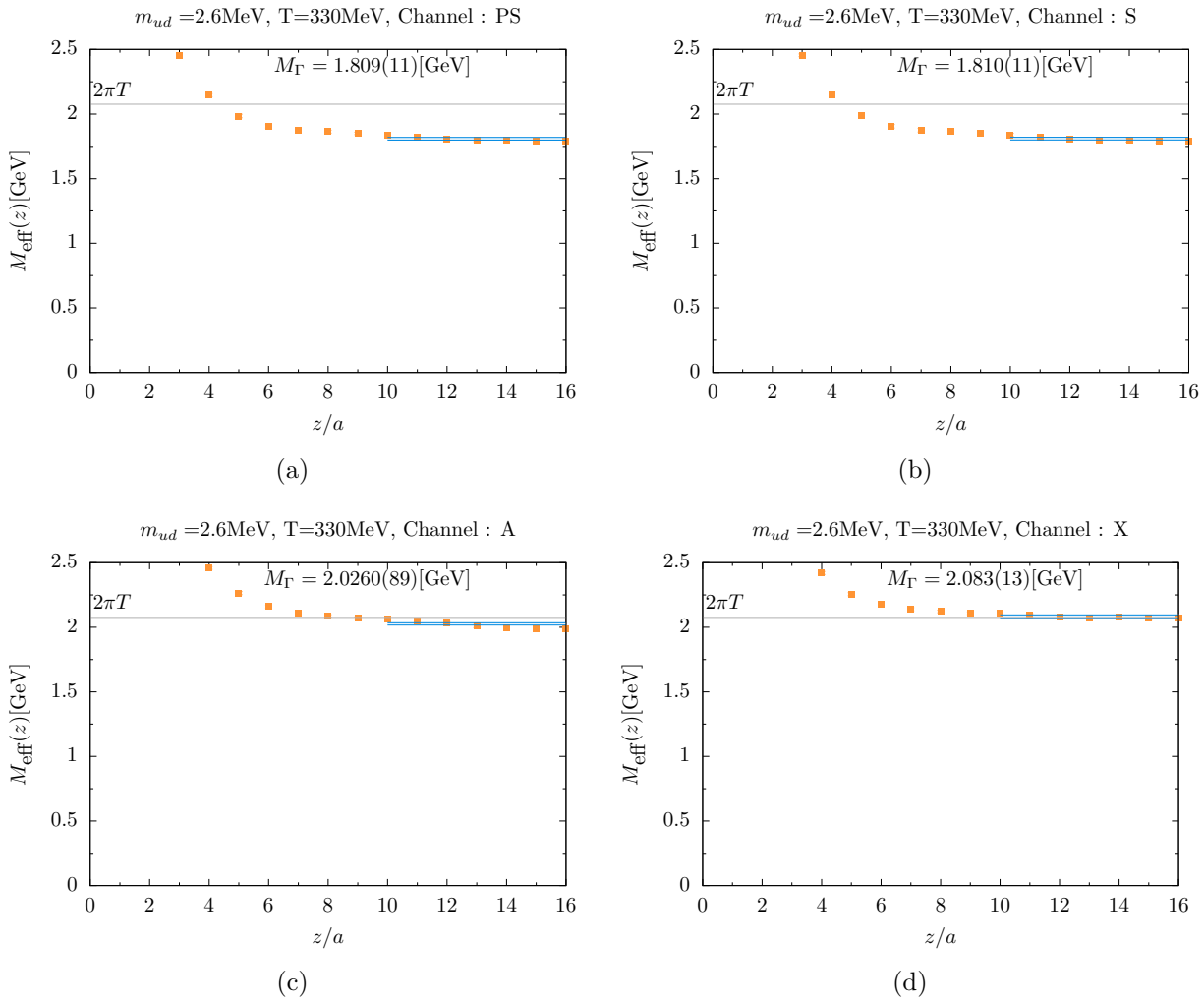

Figure 6.7: Fits compared with the effective screening mass from the $T = 330$MeV correlation function in 6.2(e).

is not present for the Möbius Domain wall fermions and so this decay remains prohibited as the isospin triplet S channel cannot decay into two PS mesons due to the exact isospin symmetry.

At higher temperatures $T > 1$GeV, [69] reported that the PS and V channels reach $\sim 1\%$ of $2\pi T$ although, their result appears to deviate from the next-to-leading order contribution from the perturbative QCD prediction, the one-loop correction to the meson mass is positive and channel independent(for related results and further details see [1, 34, 70]).

6.2.2 Screening mass difference, symmetry and temperature

Using the extracted screening masses, in addition to looking at the temperature dependence of the individual channels we also looked at the differences and how these changed with temperature as well. In contrast to the plots of the screening mass with respect to temperature, we plotted four masses of interest simultaneously to also look at how the mass difference,

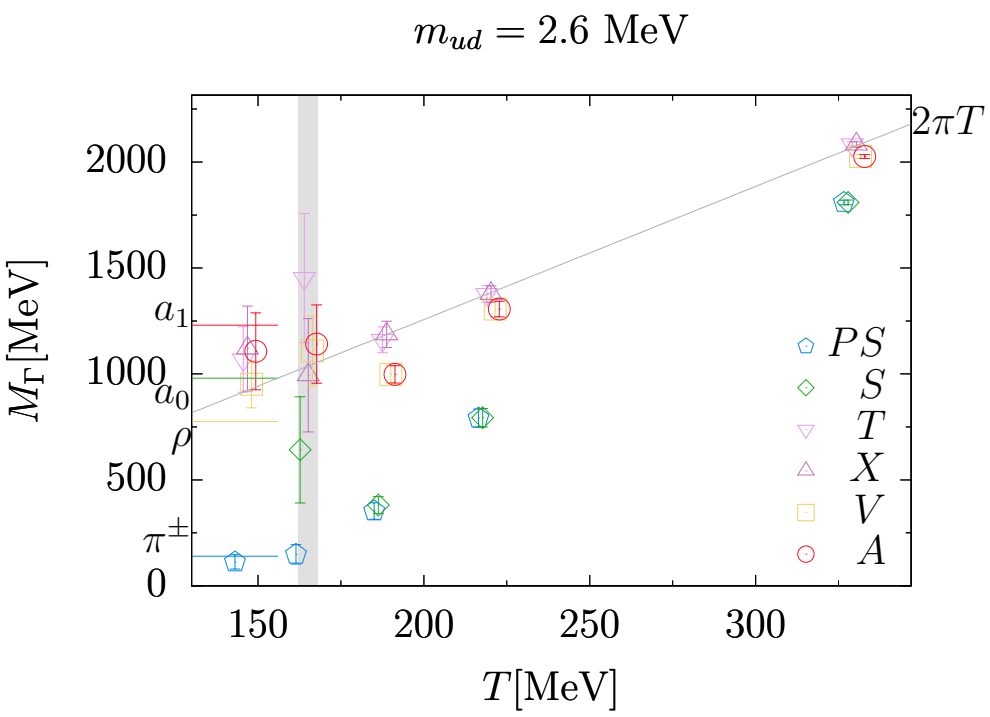

Figure 6.8: Temperature dependence in the screening masses for six meson channels corresponding the lightest mass ensemble and largest volume lattices. The grey line shows $2\pi T$, twice the groundstate Matsubara frequency. There are additional reference lines on the left corresponding to the $T = 0$ experimental results of $\pi^{\pm}, \rho, a_0$ and a_1. The grey vertical band is the estimated temperature for the chiral crossover $T_c = 165(3)$MeV. The screening mass values are horizontally offset to help readability, and are centered around the X_t, T_t channels. Note, that the X_t and T_t channels rapidly converge onto $2\pi T$ following the chiral crossover.

and thus, the symmetry behavior changes with respect to mass.

In Fig.6.10 we plotted the difference between the V and A channels Δm_{V-A}, our probe for the $SU(2)_L \times SU(2)_R$ chiral symmetry breaking, as a function of temperature. Consistent with our plots for the screening masses, these plots are all for the largest spatial lattices. The first significant feature of this plot is that the mass difference between V and A rapidly vanishes at T_c and above; while the central value is not exactly zero at T_c looking at $|\Delta m_{V-A}|/m_A$ for $am = 0.0010$, an estimator for the scale of breaking, we find that at $T = 165$MeV $\Delta m_{V-A}/m_A \sim 2.8\%$ and at the next highest temperature $T = 190$MeV $|\Delta m_{V-A}|/m_A \sim 0\%$. The small scale of the breaking at T_c due to the 3% scale of breaking is effectively restored and looking at Table 6.3 indicates that for all plotted lattices above T_c we find all of them are restored within at most a standard deviation. This observation is also aligned with evidence presented by other authors, in particular, the work by Dalla Brida et al. [1] has shown rapid drop offs in order parameters which are additional probes to chiral symmetry.

For the larger masses in this study, there is a similar behavior in the higher temperature ranges indicating that at $T \sim 220$MeV and above we see the same characteristic restoration

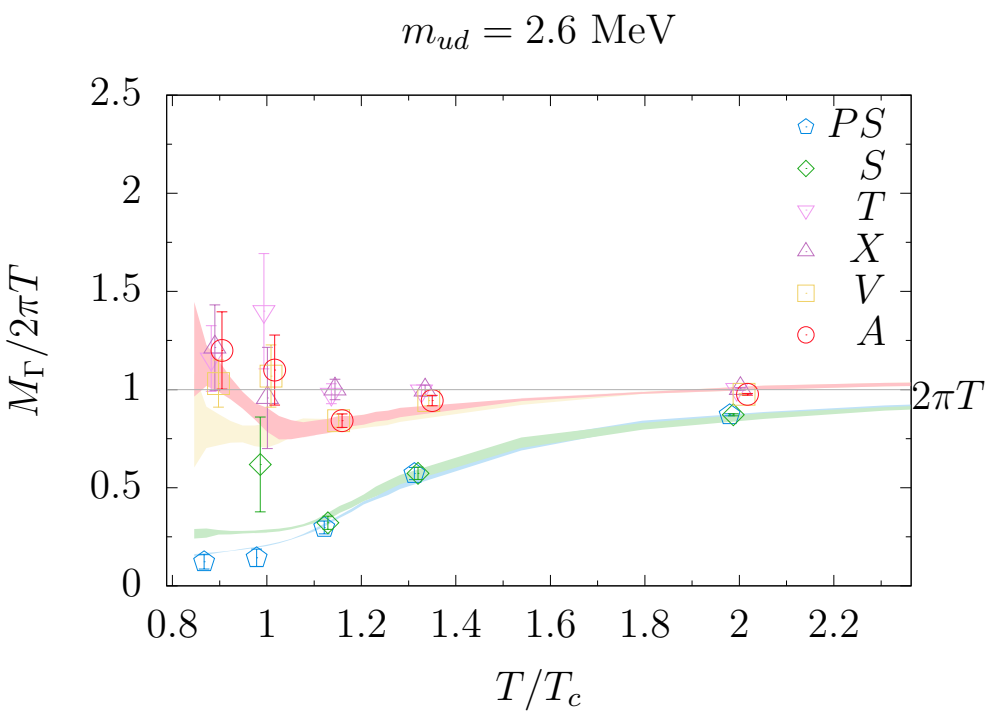

Figure 6.9: The screening masses from figure 6.8 are now normalized by $2\pi T$ and the range of temperatures are normalized by the temperature of the critical point. Using the normalized screening masses we can directly compare the $N_f = 2$ screening masses with the continuum extrapolated values from HotQCD collaboration [2] which simulated $N_f = 2 + 1$ QCD using HISQ fermions, shown as shaded bands. Due to the normalization we can see the results look consistent for all channels except the S channels due to the HISQ lattice artifact in the low temperature limit.

signatures for chiral symmetry. However, at lower temperatures there is slow convergence to zero for the two largest quark masses suggesting that the chiral crossover temperature shifts upward.

For the "restoration" of the axial $U(1)_A$ symmetry we have two probes associated with the difference between two multiplets contrsturcted from X_t and T_t, $\Delta m_{X_t - T_t}$, as well as the PS and S channels, Δm_{PS-S}. In terms of noise the difference between the tensors ($\Delta m_{X_t - T_t}$) is preferable as the signal is much more stable and not contaminated with noise from the S channel. These two screening mass differences are plotted in Figs. 6.11 and 6.12. There is an analogous behavior in both plots to that of the chiral symmetry restoration, while the error is significantly larger for both the $\Delta m_{X_t - T_t}$ Δm_{PS-S} upon reaching the chiral crossover there is rapid vanishing of the mass difference indicating, again, symmetry restoration. In the case of $U(1)_A$ there isn't a true restoration of the symmetry as this is broken by anomaly, however, the susceptbility to the topological instantons the driver of the broken axial symmetry is suppressed and thus we get an effective restoration. The restoration of $U(1)_A$ estimated from the screening mass difference is a bit larger as $\Delta m_{X_t - T_t}/m_{X_t} \sim 2(1)\%$ and $\Delta m_{PS-S}/m_S \sim 7(4)\%$ at $T = 190$MeV. At the critical point $T \sim 165$MeV this

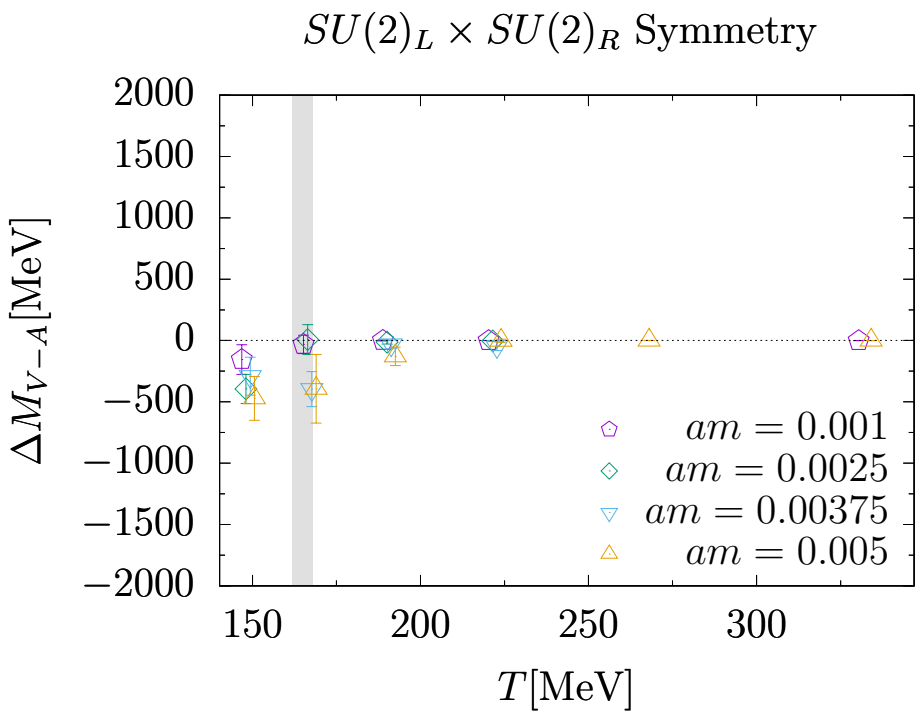

Figure 6.10: T versus ΔM_{V-A} the screening mass difference for V and A: the probe for the $SU(2)_L \times SU(2)_R$ chiral symmetry. The vertical grey band is again the estimated critical temperature for the chiral phase transition in $N_f = 2$ QCD.

is significantly larger $\Delta m_{X_t - T_t}/m_{X_t} \sim 32(36)\%$. Although the estimation of the breaking is quite large, this is still consistent with zero within error for the screening mass difference in both of our screening mass differences $\Delta m_{X_t - T_t}$ and Δm_{PS-S}. It is not clear if the symmetry is restored at the critical point, however, from this estimate we can conclude that the axial symmetry is restored around $1.15T_c$ which is consistent with our procedure for estimation of the $SU(2)_L \times SU(2)_R$ restoration as previously discussed. At temperatures $[1.15, 2.]T_c$ we find suppression of the axial anomaly effect.

Our estimates contrast with recent work in $N_f = 2 + 1$ using Möbius Domain wall fermions by Gavai et al. [34]; in their study using susceptibilities from singlet and triplet isospin PS and S operators the authors find violation of the axial $U(1)_A$ symmetry above the chiral crossover and reported broken axial symmetry up to $T = 186$MeV. However, their lattice is quite coarse at $a > 0.13fm$ which is coarser than a previous study by JLQCD [22] $a \sim 0.1$fm. In the case of the study by JLQCD, the authors found violation of the Ginsparg-Wilson relation by low lying eignemodes in the Dirac operator which exceeded the residual mass leading to an over estimation of the $U1(1)_A$ anomaly.

Due to our study of $N_f = 2$ QCD at fixed lattice spacing we are unable to make a more precise determination of the exact temperature of restoration of the axial symmetry. For the higher masses in the study we also cannot draw meaningful conclusions about the behavior of the anomaly as we can see the see an analogous trend to the $SU(2)_L \times SU(2)_R$ restoration with a milder temperature dependent trend below the chiral crossover. However,

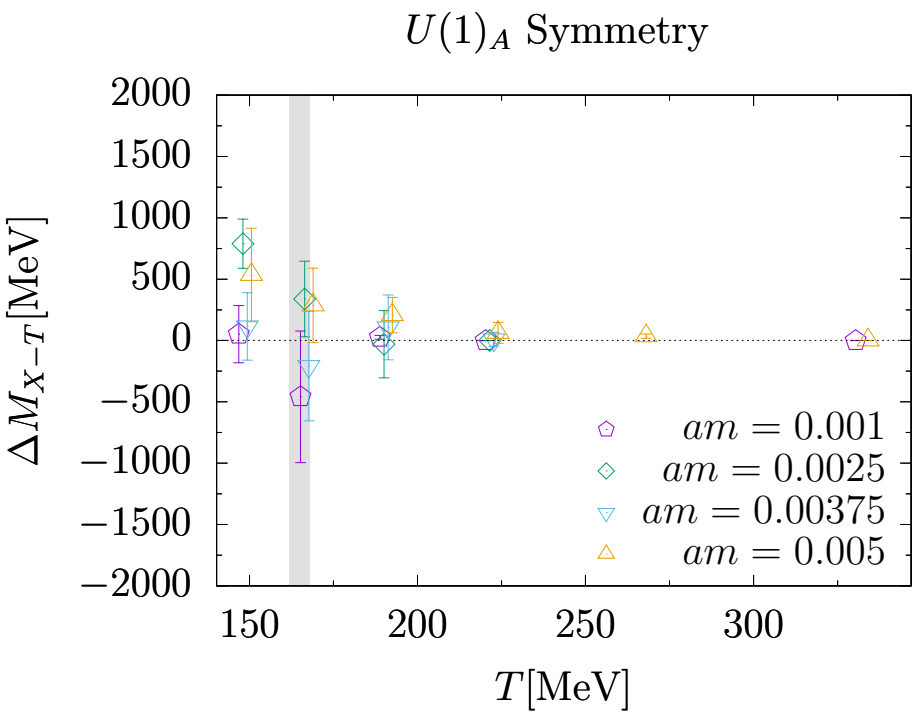

Figure 6.11: T versus ΔM_{X-T} the screening mass difference between the temporal tensor channels X_t and T_t: one of the probes for $U(1)_A$ symmetry. The vertical grey band is the estimated critical temperature in $N_f = 2$ QCD.

to more precisely determine the temperature threshold for axial symmetry restoration, which is important in determining the universality of the chiral phase transition, we would need additional lattices with different spacings to achieve a more fine scale of resolution slightly above T_c.

In addition to probes for $SU(2)_L \times SU(2)_R$ and $U(1)_A$ there is also a series mass difference which serve as probes for the emergent $SU(2)_{CS}$ which was described in section 5.2. In figure 6.13, we plotted the screening mass difference between the A and X_t channels, Δm_{A-X_t}, one probe for $SU(2)_{CS}$. As the $SU(2)_{CS}$ symmetry is an approximate symmetry up to $\mathcal{O}(1/T)$ we do not expect an exact zero for the screening mass difference within the temperature range for such an emergent symmetry. We do, however, expect that our estimators for the scale of the symmetry breaking should reach similar thresholds to the other symmetries. In figure 6.13, consistent with the $SU(2)_L \times SU(2)_R$ and $U(1)_A$ we see a reduction in noise with increasing temperature. However, there is a qualitative difference in the behavior of Δm_{A-X_t}, while the other symmetries of the mesons monotonically vanished, the probe for $SU(2)_{CS}$ increases and then flips sign before decreasing. Although the plot of Δm_{A-X_t} appears to be vanishing, in Fig. 6.14 we find a significant different at the highest temperature $T = 330$MeV. In figure 6.14, we plot $SU(2)_L \times SU(2)_R$(green pentagons), $U(1)_A$ ($PS-S$ purple rhombuses, $X_t - T_t$ lower blue triangles) and $SU(2)_{CS}$ (upper yellow triangles); whereas the first three set of points are consistent with zero to within ~ 1MeV and represent less than $\sim 1\%$ from the proportion of the screening mass difference with respect to temperature, the quantity

m_{A-X_t} is on the order of ~ 50MeV with separation from zero of roughly 4σ corresponding to the small estimated error from the fit. Despite this large separation we can estimate that the symmetry is still approximate as $|\Delta m_{A-X_t}|/T \sim 0.17(3)$. This does conflict with the observation of approximate emergence made in [15, 14] where evidence for $SU(2)_{CS}$ from $T \sim 200$MeV was presented. The approximate order of the symmetry may be consistent within the temperature window estimated in [25], however, the "quality" of the approximate symmetry exceeds the threshold for $T \gtrapprox 326$MeV which is estimated to be around 0.15 in the article.

6.2.3 Systematics for finite volume and temperature

Beginning with the estimation of the systematic error in our study let us turn our attention to finite volume effects for the three temperatures $T = 147, 165$ and 220MeV. All three temperatures are plotted in Fig. 6.15, between the different lattice sizes we do not see separation more than 2σ between screening masses from smallest to largest spatial extents. Again, the S channel in Fig. 6.15(b), is the exception around the critical point as the smallest lattice volume point was omitted by our fitting criteria.

As our study was done using a single fixed lattice spacing, we cannot numerically estimate the discretization effects. Despite this, our choice of a relatively fine lattice compared with other groups and our correspondence with the HotQCD result in the continuum does bolster

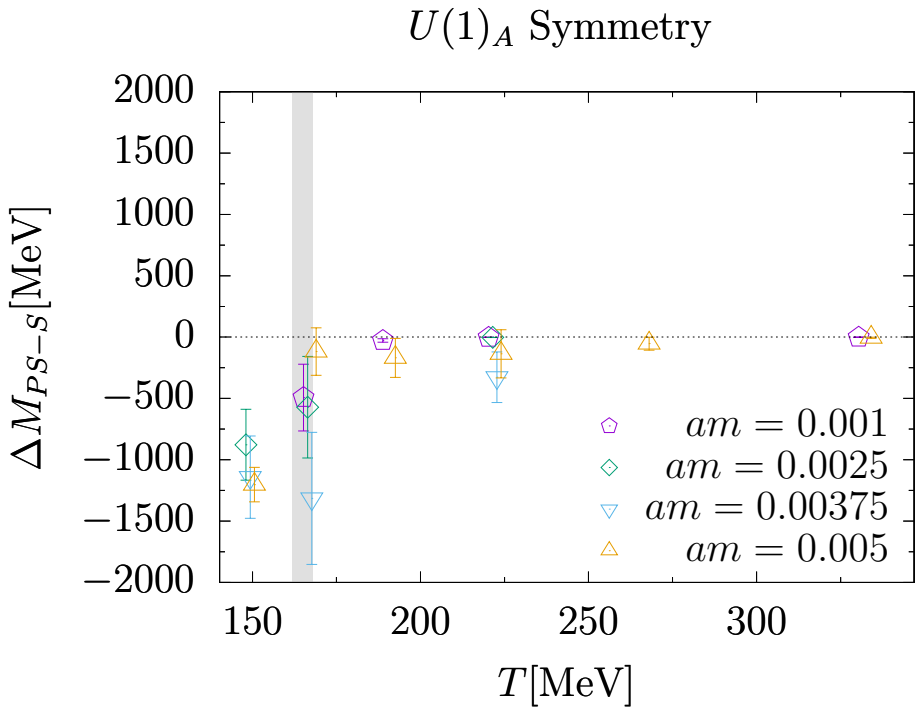

Figure 6.12: T versus ΔM_{PS-S} the screening mass difference between the PS and S: another one of the probes for $U(1)_A$ symmetry. The vertical grey band is the estimated critical temperature in $N_f = 2$ QCD.

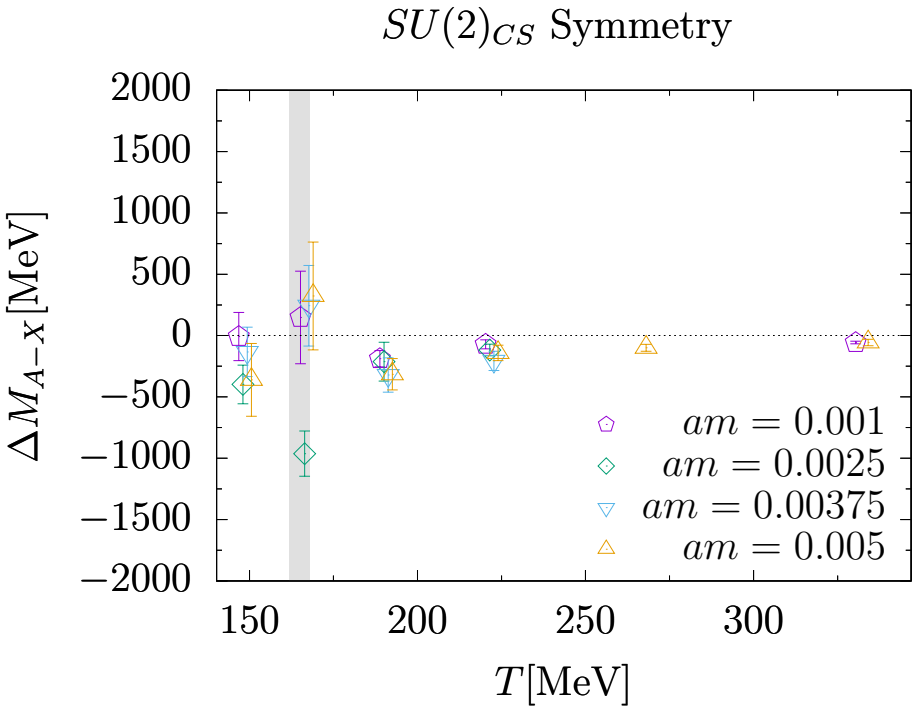

Figure 6.13: T versus ΔM_{A-X_t} the screening mass difference between the vector channel A and the temporal tensor X_t: one of the probes for the $SU(2)_{CS}$ symmetry. The vertical grey band is the estimate critical temperature for the chiral crossover in $N_f = 2$ QCD.

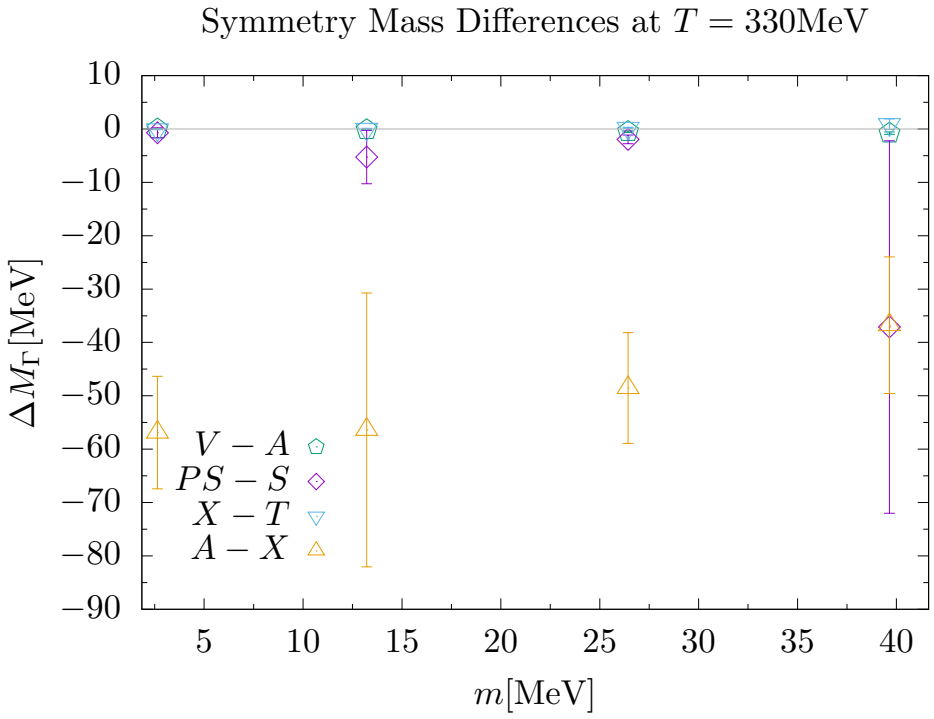

Figure 6.14: Simultaneous plot of the screening mass differences ΔM_{V-A}(pentagons), ΔM_{PS-S}(rhombuses), $\Delta M_{X_t-T_t}$(lower triangles) and ΔM_{A-X_t}(upper triangles) and their quark mass dependence at $T = 330$MeV. Compared with the first three which probe $SU(2)_L \times SU(2)_R$ and $U(1)_A$ respectively, and show consistency with zero to within error on the order of ~ 1MeV(for all probes up to the heaviest quarks), ΔM_{A-X_t} shows quite a significant difference of between $\sim 40 - 50$MeV. The associated chiral symmetry is approximate at all masses, with $|\Delta M_{A-X}|/T \sim 0.17(3)$ at 2.6MeV and appears to get better with increased mass as the 39MeV ensemble is $|\Delta M_{A-X}|/T \sim 0.11(4)$.

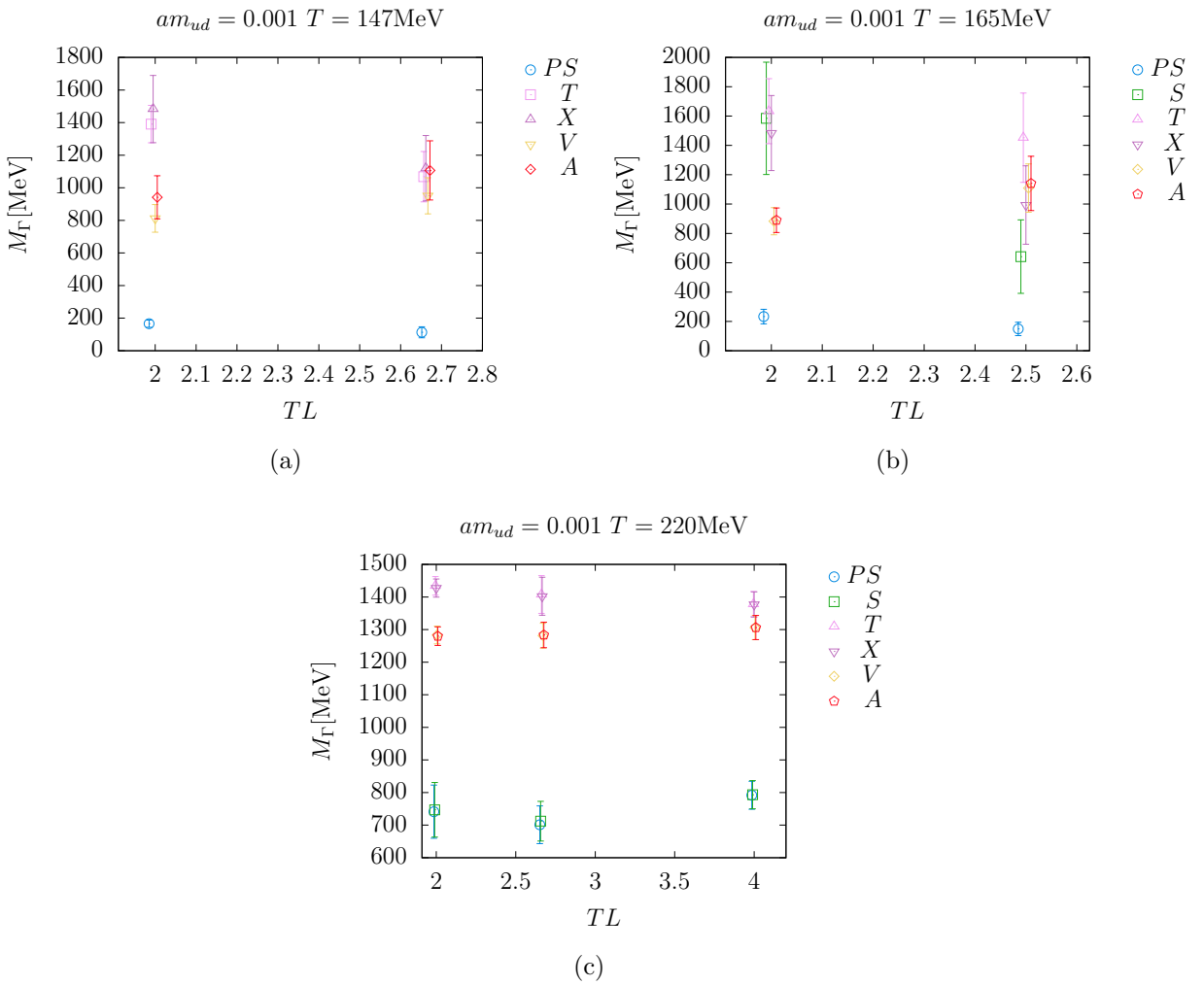

Figure 6.15: Lattice aspect ratio TL versus screening mass (M_Γ) at temperatures $= 147, 165$ and 220MeV. Volume dependent effects are not significant as the screening masses do not deviate more than 2σ.

some confidence in our results. Due to our choice of fine lattice we also expect the $\mathcal{O}(a)$ improvement due to the chiral symmetry of the Möbius Domain Wall fermion action.

It is also important to note that our range of up and down quark masses covers the physical point, in addition to which, the lightest quarks sufficiently close to the chiral limit are approximately physical with 71% of the mass of the physical up and down quarks.

$L^3 \times L_t$	T[MeV]	am	m[MeV]	m_S	m_{PS}	m_V	m_A	m_X	m_T
$48^3 \times 18$	147	0.00100	2.6		113(34)	951(111)	1106(182)	1120(201)	1068(154)
		0.00250	6.6	1097(288)	220(5)	1009(69)	1404(129)	1801(166)	1012(71)
		0.00375	9.9	1387(337)	245(5)	854(74)	1145(155)	1279(223)	1164(97)
		0.00500	13.2		135(7)	903(58)	1375(177)	1733(281)	1199(117)
$36^3 \times 18$	147	0.00100	2.6		166(22)	812(85)	941(132)	1483(206)	1391(115)
		0.00250	6.6	2605(533)	220(12)	767(53)	930(156)	1645(153)	1228(117)
		0.00375	9.9	1586(333)	240(11)	886(77)	1046(181)	1635(107)	1216(52)
		0.00500	13.2	1490(139)	288(6)	861(43)	1231(125)	1527(117)	1091(56)
$40^3 \times 16$	165	0.00100	2.6	642(251)	149(46)	1109(165)	1141(185)	994(268)	1453(305)
		0.00250	6.6	817(402)	245(18)	544(146)	536(201)	1499(196)	1161(146)
		0.00375	9.9		301(16)	1003(90)	1400(158)	1156(305)	1364(171)
		0.00500	13.2		273(20)	936(113)	1330(216)	1007(341)	721(95)
$32^3 \times 16$	165	0.00100	2.6		233(49)	883(93)	890(84)	1485(256)	1633(222)
		0.00250	6.6		362(53)	904(75)	978(133)	1268(431)	1212(176)
		0.00375	9.9	1624(538)	309(14)	934(90)	1047(131)	1552(178)	966(152)
		0.00500	13.2	444(187)	326(24)	932(84)	1106(159)	1679(207)	1216(89)
$32^3 \times 14$	189	0.00100	2.6	381(40)	353(39)	998(40)	998(41)	1187(62)	1161(61)
		0.00250	6.6		362(39)	1150(49)	1164(52)	1376(154)	1407(131)
		0.00375	9.9		402(27)	964(33)	996(44)	1318(146)	1212(135)
		0.00500	13.2	582(159)	413(29)	940(44)	1069(74)	1385(114)	1178(82)
$48^3 \times 12$	220	0.00100	2.6	793(43)	792(43)	1306(37)	1306(37)	1377(39)	1378(39)
		0.00250	6.6	913(21)	911(20)	1290(39)	1293(39)	1411(38)	1410(38)
		0.00375	9.9	1033(192)	706(47)	1189(78)	1235(93)	1441(48)	1431(54)
		0.00500	13.2	888(108)	752(109)	1234(33)	1236(35)	1378(58)	1316(48)
$40^3 \times 12$	220	0.00500	13.2	1534(351)	502(51)	1327(32)	1298(28)	1291(116)	1425(38)
		0.01000	26.4	1495(336)	696(35)	1222(24)	1275(32)	1302(106)	1444(99)
$32^3 \times 12$	220	0.00100	2.6	712(61)	701(58)	1281(38)	1283(39)	1402(58)	1408(58)
		0.00250	6.6	697(88)	797(85)	1235(22)	1234(23)	1294(46)	1307(51)
		0.00375	9.9	615(158)	696(77)	1244(23)	1251(24)	1570(103)	1374(104)
		0.00500	13.2	1350(360)	717(90)	1182(25)	1213(23)	1465(115)	1292(69)
		0.01000	26.4	1254(226)	686(36)	1227(57)	1160(76)	1345(101)	1302(80)
$24^3 \times 12$	220	0.00100	2.6	747(84)	741(82)	1283(27)	1280(29)	1427(28)	1434(28)
		0.00250	6.6	1637(334)	806(121)	1292(30)	1295(30)	1345(77)	1305(80)
		0.00375	9.9	687(120)	785(53)	1333(32)	1335(33)	1392(32)	1398(32)
		0.00500	13.2	2505(488)	736(134)	1219(31)	1245(36)	1327(66)	1469(55)
		0.01000	26.4	770(153)	713(54)	1271(29)	1307(38)	1421(33)	1450(29)
$32^3 \times 10$	264	0.00500	13.2	1319(35)	1266(26)	1566(18)	1566(18)	1666(32)	1631(26)
		0.00800	21.1	1252(19)	1251(19)	1572(15)	1574(15)	1626(19)	1627(20)
		0.01000	26.4	1525(121)	1117(94)	1560(19)	1581(27)	1630(49)	1654(28)
		0.01500	39.6	1458(123)	1236(100)	1596(21)	1599(21)	1666(28)	1693(29)
$32^3 \times 8$	330	0.00100	2.6	1810(11)	1809(11)	2026(9)	2026(9)	2083(13)	2083(13)
		0.00500	13.2	1796(19)	1791(18)	2038(12)	2038(12)	2094(24)	2094(24)
		0.01000	26.4	1783(15)	1781(15)	2033(8)	2033(8)	2082(9)	2082(9)
		0.01500	39.6	1828(24)	1791(22)	2027(10)	2028(10)	2064(17)	2063(17)
		0.02000	52.9	1807(15)	1796(14)	2013(18)	2014(18)	2069(15)	2066(15)
		0.04000	105.7	1824(27)	1770(20)	2021(16)	2024(16)	2080(16)	2073(15)

Table 6.2: Meson screening masses in physical units [MeV] for various channels extracted from combinations of fit and effective mass, using the cosh ansatz, associated with the correlators. Empty data indicates omitted values due to poor fit or an unstable correlation curve for the range of fit.

$L^3 \times L_t$	T[MeV]	am	m[MeV]	m_{PS-S}	m_{V-A}	m_{X-T}	m_{A-X}
$48^3 \times 18$	147	0.00100	2.6		-155(120)	52(233)	-8(196)
		0.00250	6.6	-877(289)	-395(119)	789(201)	-398(158)
		0.00375	9.9	-1141(335)	-291(155)	115(274)	-133(201)
		0.00500	13.2		-472(179)	534(381)	-361(297)
$36^3 \times 18$	147	0.00100	2.6		-129(66)	92(290)	-539(213)
		0.00250	6.6	-2385(525)	-163(139)	417(235)	-710(169)
		0.00375	9.9	-1346(331)	-160(171)	419(127)	-586(114)
		0.00500	13.2	-1203(141)	-370(127)	437(147)	-296(144)
$40^3 \times 16$	165	0.00100	2.6	-493(272)	-32(75)	-459(536)	148(377)
		0.00250	6.6	-572(414)	8(121)	338(307)	-963(184)
		0.00375	9.9		-397(143)	-208(447)	244(329)
		0.00500	13.2		-394(279)	287(304)	323(439)
$32^3 \times 16$	165	0.00100	2.6		-7(28)	-149(464)	-595(281)
		0.00250	6.6		-74(151)	56(542)	-290(445)
		0.00375	9.9	-1315(539)	-113(128)	586(247)	-505(248)
		0.00500	13.2	-118(194)	-174(138)	463(221)	-573(227)
$32^3 \times 14$	189	0.00100	2.6	-28(14)	0(4)	26(16)	-188(67)
		0.00250	6.6		-14(16)	-30(274)	-213(159)
		0.00375	9.9		-32(35)	107(265)	-321(140)
		0.00500	13.2	-169(159)	-129(75)	207(144)	-315(127)
$48^3 \times 12$	220	0.00100	2.6	-2(1)	-0(0)	-1(0)	-71(37)
		0.00250	6.6	-2(1)	-3(1)	0(1)	-118(47)
		0.00375	9.9	-327(206)	-46(35)	10(57)	-206(79)
		0.00500	13.2	-136(196)	-2(13)	62(86)	-141(62)
$40^3 \times 12$	220	0.00500	13.2	-1032(399)	14(18)	-22(96)	-141(98)
		0.01000	26.4	-799(347)	-48(20)	-2(79)	-87(79)
$32^3 \times 12$	220	0.00100	2.6	-11(7)	-2(2)	-5(4)	-119(80)
		0.00250	6.6	100(102)	1(2)	-13(32)	-60(36)
		0.00375	9.9	81(109)	-6(2)	197(195)	-320(98)
		0.00500	13.2	-633(444)	-31(17)	173(135)	-252(112)
		0.01000	26.4	-568(243)	67(79)	44(131)	-185(124)
$24^3 \times 12$	220	0.00100	2.6	-6(4)	4(4)	-7(5)	-148(38)
		0.00250	6.6	-831(225)	-3(2)	40(67)	-48(97)
		0.00375	9.9	98(74)	-1(1)	-6(6)	-56(43)
		0.00500	13.2	-1769(375)	-26(15)	-144(111)	-81(78)
		0.01000	26.4	-57(114)	-36(23)	-28(36)	-115(45)
$32^3 \times 10$	264	0.00500	13.2	-53(53)	-1(1)	35(18)	-100(28)
		0.00800	21.1	-0(3)	-1(1)	-0(3)	-53(20)
		0.01000	26.4	-407(203)	-21(26)	-25(67)	-49(69)
		0.01500	39.6	-222(217)	-3(1)	-27(28)	-67(30)
$32^3 \times 8$	330	0.00100	2.6	-1(1)	-0(0)	-0(0)	-57(11)
		0.00500	13.2	-5(5)	-0(0)	0(0)	-56(26)
		0.01000	26.4	-2(1)	-0(0)	0(0)	-49(10)
		0.01500	39.6	-37(35)	-1(0)	1(1)	-37(13)
		0.02000	52.9	-12(6)	-2(0)	2(1)	-54(12)
		0.04000	105.7	-54(30)	-4(2)	6(3)	-55(11)

Table 6.3: Screening mass differences as the probes for various symmetries are listed in physical units [MeV]. Because these values are dependent on the screening masses in Table 6.2, any omitted values cannot be used in the difference of screening mass and so are not reported.

Chapter 7

Summary and Conclusion

Having simulated $N_f = 2$ QCD with Möbius domain wall fermions, in the previous chapter we find that the probes for the chiral symmetry, the screening mass differences drawn from the correlation function by combination effective mass and fit indicate we can easily study the behaviors of chiral symmetry around the critical temperature T_c with a straightforward method of analysis. The roots of this which we have covered in chapter 3, are in the approximation of the Overlap operator by way of the domain wall fermions for which we choose specifically the form of the Möbius domain wall fermion kernel. This assured us a theoretically exact form of the chiral symmetry for which the scale of breaking represented by the residual mass was well under control with $m_{res} \sim 0.14$MeV. Due to this we expected to find good agreement with high quality study done by HotQCD, as shown in chapter 6 we found excellent agreement between our ensembles for the $am = 0.0010$ quarks with their continuum extrapolated result from [2]. In particular we find that our restoration behaviors coincide for the $SU(2)_L \times SU(2)_R$ symmetry at the respective T_c values as their study was done for $N_f = 2 + 1$ flavor structure. In the future we hope to have high quality $N_f = 2 + 1$ data which will allow an additional and direct comparison, although this work by JLQCD is ongoing.

Along with the restoration of the vector like chiral symmetries we also found evidence of suppression of topological instantonic effect at temperatures $T > T_c$ supporting our initial assertion that previous work which studied the instantonic gas, and showed $T \sim T_c$ has significant instantonic effects driving $U(1)_A$ breaking, is not favored in the case of degenerate light quarks. From our simulations data we do see quite a good signal for restoration of $U(1)_A$ at $T \sim 190$MeV $T = 1.15T_c$, which would indicate that the topological gluon fluctuations are suppressed quite close to T_c if not at the critical temperature itself. Unfortunately this work was not able to elucidate an exact point of transition and so some ambiguity remains as to whether the restoration of $U(1)_A$ is coincident with the restoration of chiral symmetry. However, based on the scale of breaking at T_c of $\sim 32(37)\%$ versus the scale of the estimate for the residual screening mass difference at $T = 1.15T_c(189\text{MeV})$ of $\sim 2(1)\%$ and $\sim 7(4)\%$ it is possible that we do have restoration at T_c, which would be consonant with more recent work [6, 4, 24].

For this study of $N_f = 2$ QCD we chose a range of $[0.9T_c, 2.0T_c]$ to assess behaviors of the quarks for several different finite temperature regimes. With resepect to the thermal beahviors of the screening mass we find several interesting features; first of which, we find

that as high as $0.9T_c$ we find the lightest quarks $am = 0.0010$, which represents $\sim 71\%$ of the physical point mass, are consistent with the $T = 0$ experimental values. Implying the scale of the chiral symmetry breaking from the chiral condensate is rapid upon crossing the chiral crossover. Additionally this indicates that chiral symmetry breaking effects are quite strong even into the high temperature region below T_c. Our second key feature in the screening mass thermal dependence, upon crossing the critical temperature the S, A, and X_t channels reduce in mass and become degenerate with their $SU(2)_L \times SU(2)_R$ or $U(1)_A$ partners PS,V and T_t. After which as we increase in temperature toward $2T_c$ the channels begin to monotonically converge to twice the long range Matsubara groundstate mass $2\pi T$. This behavior is the most dramatically visible in the temporal tensor channels X_t and T_t, as these immediately converge to $2\pi T$ upon crossing T_c. While the temperatures are too low to check the leading order correction to the high temperature screening mass perturbative result predicted from NRQCD$_3$ [12], as the work done by Dalla Brida et al [1] showed these corrections are accessible to lattice studies at very high temperatures $\sim \mathcal{O}(100)$GeV. In fact, their observation is that even at such high temperatures the corrections from spin dependent effects which appear at all temperatures from the $\mathcal{O}(g^4T)$ contribution to the screening mass, are significant enough to maintain small deviations from the $2\pi T$ limit of the screening masses. This would seem to contrast to the effect seen in the temporal tensor channels, however, for the tensors such spin dependent corrections would be suppressed by the scale of the screening mass for such heavy channels. This may actually make the the tensors an excellent probe for the scale of separation from $2\pi T$ with lighter channels in additional high temperature studies of the thermal properties of the spatial screening mass.

The effective theory framework in studying the high temperature limits of the free quark propagator in QCD which we discussed in chapter 4 is effective in describing the thermal properties of the screening mass, and shows that the first two terms of the screening mass remain spin independent. Therefore, we would expect that at high temperatures we would see an approximate symmetry arising from this degeneracy of the screening mass. To this end in chapter 5 and 6 we discussed an analogous symmetry to the $T = 0$ heavy quark isospin symmetry which applies to the high temperature limit the $SU(2)_{CS}$. This approximate symmetry arising from the leading order contribution to the screening mass was previously observed at temperatures $T \sim 2T_c$ [15]. In our study of the same temperature range using the screening masses as opposed to a proportion of the correlators, we found weak evidence for the emergence of the approximate symmetry at $T = 2T_c$; following our argument from the free quark correlator it is very likely such an approximate symmetry does exist, but likely at higher temperatures than previous evidence suggested. Our estimation of the symmetry difference in proportion to the scale of the thermal mass suggests that a -60MeV difference between the A and X_t channels is $\sim 17\%$ which makes the symmetry, at best, approximate. However, from the arguments made in [25], we would expect a better quality of the symmetry at $T = 330$MeV; this suggests that we could be just below the threshold for $SU(2)_{CS}$. Our work directly contrasts the claims made about the claims of $SU(2)_{CS}$ as part of a more symmetric confined quark phase which sets in upon resotration of chiral symmetry. We might instead make a more modest claim that this emergent symmetry is a consequence of scale of spin dependent contributions to the screening mass being suppressed below $\mathcal{O}(100)$GeV, where such a term only contributes a few percent as per the argument made in [1].

Bibliography

[1] M. Dalla Brida, L. Giusti, T. Harris, D. Laudicina and M. Pepe, *Non-perturbative thermal QCD at all temperatures: the case of mesonic screening masses*, *JHEP* **04** (2022) 034 [2112.05427].

[2] A. Bazavov et al., *Meson screening masses in (2+1)-flavor QCD*, *Phys. Rev. D* **100** (2019) 094510 [1908.09552].

[3] R.D. Pisarski and F. Wilczek, *Remarks on the Chiral Phase Transition in Chromodynamics*, *Phys. Rev. D* **29** (1984) 338.

[4] S. Aoki, H. Fukaya and Y. Taniguchi, *Chiral symmetry restoration, eigenvalue density of Dirac operator and axial U(1) anomaly at finite temperature*, *Phys. Rev. D* **86** (2012) 114512 [1209.2061].

[5] JLQCD collaboration, *Role of the axial U(1) anomaly in the chiral susceptibility of QCD at high temperature*, *PTEP* **2022** (2022) 023B05 [2103.05954].

[6] JLQCD collaboration, *Chiral susceptibility and axial U(1) anomaly near the (pseudo-)critical temperature*, *PoS* **LATTICE2023** (2024) 184 [2401.06459].

[7] G. Cossu, S. Aoki, H. Fukaya, S. Hashimoto, T. Kaneko, H. Matsufuru et al., *Finite temperature study of the axial U(1) symmetry on the lattice with overlap fermion formulation*, *Phys. Rev. D* **87** (2013) 114514 [1304.6145].

[8] T. Schäfer and E.V. Shuryak, *Instantons in QCD*, *Rev. Mod. Phys.* **70** (1998) 323 [hep-ph/9610451].

[9] D. Diakonov and V.Y. Petrov, *CHIRAL CONDENSATE IN THE INSTANTON VACUUM*, *Phys. Lett. B* **147** (1984) 351.

[10] D.J. Gross, R.D. Pisarski and L.G. Yaffe, *QCD and Instantons at Finite Temperature*, *Rev. Mod. Phys.* **53** (1981) 43.

[11] A. Ringwald and F. Schrempp, *Confronting instanton perturbation theory with QCD lattice results*, *Phys. Lett. B* **459** (1999) 249 [hep-lat/9903039].

[12] M. Laine and M. Vepsalainen, *Mesonic correlation lengths in high temperature QCD*, *JHEP* **02** (2004) 004 [hep-ph/0311268].

[13] C. Rohrhofer, *Symmetries of QCD at high temperature*, Ph.D. thesis, Graz U., Graz U., 2018.

[14] C. Rohrhofer, Y. Aoki, L.Y. Glozman and S. Hashimoto, *Chiral-spin symmetry of the meson spectral function above T_c*, *Phys. Lett. B* **802** (2020) 135245 [1909.00927].

[15] C. Rohrhofer, Y. Aoki, G. Cossu, H. Fukaya, C. Gattringer, L.Y. Glozman et al., *Symmetries of spatial meson correlators in high temperature QCD*, *Phys. Rev. D* **100** (2019) 014502 [1902.03191].

[16] L.Y. Glozman, O. Philipsen and R.D. Pisarski, *Chiral spin symmetry and the QCD phase diagram*, *Eur. Phys. J. A* **58** (2022) 247 [2204.05083].

[17] L.Y. Glozman, *Chiralspin symmetry and QCD at high temperature*, *Eur. Phys. J. A* **54** (2018) 117 [1712.05168].

[18] L.Y. Glozman, *$SU(2N_F)$ symmetry of QCD at high temperature and its implications*, *Acta Phys. Polon. Supp.* **10** (2017) 583 [1610.00275].

[19] L.Y. Glozman, *SU(4) symmetry of the dynamical QCD string and genesis of hadron spectra*, *Eur. Phys. J. A* **51** (2015) 27 [1407.2798].

[20] N. Brambilla, A. Pineda, J. Soto and A. Vairo, *Effective Field Theories for Heavy Quarkonium*, *Rev. Mod. Phys.* **77** (2005) 1423 [hep-ph/0410047].

[21] M. Neubert, *Heavy quark symmetry*, *Phys. Rept.* **245** (1994) 259 [hep-ph/9306320].

[22] JLQCD collaboration, *Violation of chirality of the Möbius domain-wall Dirac operator from the eigenmodes*, *Phys. Rev. D* **93** (2016) 034507 [1510.07395].

[23] A. Tomiya, G. Cossu, S. Aoki, H. Fukaya, S. Hashimoto, T. Kaneko et al., *Evidence of effective axial U(1) symmetry restoration at high temperature QCD*, *Phys. Rev. D* **96** (2017) 034509 [1612.01908].

[24] JLQCD collaboration, *Study of the axial $U(1)$ anomaly at high temperature with lattice chiral fermions*, *Phys. Rev. D* **103** (2021) 074506 [2011.01499].

[25] T.-W. Chiu, *Symmetries of meson correlators in high-temperature QCD with physical (u/d,s,c) domain-wall quarks*, *Phys. Rev. D* **107** (2023) 114501 [2302.06073].

[26] T.-W. Chiu, *Symmetries of spatial correlators of light and heavy mesons in high temperature lattice QCD*, *Phys. Rev. D* **110** (2024) 014502 [2404.15932].

[27] JLQCD collaboration, *Symmetry of screening masses of mesons in two-flavor lattice QCD at high temperatures*, *Phys. Rev. D* **111** (2025) 114506 [2501.12675].

[28] D. Ward, S. Aoki, Y. Aoki, H. Fukaya, S. Hashimoto, I. Kanamori et al., *Study of symmetries in finite temperature $N_f = 2$ QCD with Mobius Domain Wall Fermions*, *PoS* **LATTICE2024** (2025) 346 [2412.06574].

[29] D. Ward, S. Aoki, Y. Aoki, H. Fukaya, S. Hashimoto, I. Kanamori et al., *Study of Chiral Symmetry and $U(1)_A$ using Spatial Correlators for N_f = 2 + 1 QCD at finite temperature with Domain Wall Fermions*, *PoS* **LATTICE2023** (2024) 182 [2401.07514].

[30] JLQCD collaboration, *Axial U(1) symmetry and mesonic correlators at high temperature in $N_f = 2$ lattice QCD*, *PoS* **LATTICE2019** (2020) 178 [2001.07962].

[31] JLQCD collaboration, *Axial U(1) symmetry near the pseudocritical temperature in $N_f = 2 + 1$ lattice QCD with chiral fermions*, *PoS* **LATTICE2023** (2024) 185 [2401.14022].

[32] JLQCD collaboration, *Characterizing Strongly Interacting Matter at Finite Temperature: (2+1)-Flavor QCD with Möbius Domain Wall fermions*, *PoS* **LATTICE2023** (2024) 187.

[33] JLQCD collaboration, *Topological Susceptibility in $N_f = 2$ QCD at Finite Temperature*, *EPJ Web Conf.* **175** (2018) 07024 [1711.07537].

[34] R.V. Gavai, M.E. Jaensch, O. Kaczmarek, F. Karsch, M. Sarkar, R. Shanker et al., *Aspects of the chiral crossover transition in (2+1)-flavor QCD with Möbius domain-wall fermions*, *Phys. Rev. D* **111** (2025) 034507 [2411.10217].

[35] S.L. Adler, *Axial vector vertex in spinor electrodynamics*, *Phys. Rev.* **177** (1969) 2426.

[36] J.S. Bell and R. Jackiw, *A PCAC puzzle: $\pi^0 \to \gamma\gamma$ in the σ model*, *Nuovo Cim. A* **60** (1969) 47.

[37] M.F. Atiyah and I.M. Singer, *The Index of elliptic operators. 1*, *Annals Math.* **87** (1968) 484.

[38] M.F. Atiyah and I.M. Singer, *The Index of elliptic operators. 5.*, *Annals Math.* **93** (1971) 139.

[39] G. 't Hooft, *Symmetry Breaking Through Bell-Jackiw Anomalies*, *Phys. Rev. Lett.* **37** (1976) 8.

[40] T.D. Cohen, *The High temperature phase of QCD and U(1)-A symmetry*, *Phys. Rev. D* **54** (1996) R1867 [hep-ph/9601216].

[41] T.D. Cohen, *The Spectral density of the Dirac operator above T(c) rep*, in *APCTP Workshop on Astro-Hadron Physics: Properties of Hadrons in Matter*, pp. 100–114, 10, 1997 [nucl-th/9801061].

[42] A. Pelissetto and E. Vicari, *Relevance of the axial anomaly at the finite-temperature chiral transition in QCD*, *Phys. Rev. D* **88** (2013) 105018 [1309.5446].

[43] T. Kanazawa and N. Yamamoto, *Quasi-instantons in QCD with chiral symmetry restoration*, *Phys. Rev. D* **91** (2015) 105015 [1410.3614].

[44] T. Sato and N. Yamada, *Linking $U(2) \times U(2)$ to $O(4)$ model via decoupling*, *Phys. Rev. D* **91** (2015) 034025 [1412.8026].

[45] H.J. Rothe, *Lattice Gauge Theories*, WORLD SCIENTIFIC, 3rd ed. (2005), 10.1142/5674.

[46] L.H. Karsten and J. Smit, *Lattice Fermions: Species Doubling, Chiral Invariance, and the Triangle Anomaly*, *Nucl. Phys. B* **183** (1981) 103.

[47] H.B. Nielsen and M. Ninomiya, *No Go Theorem for Regularizing Chiral Fermions*, *Phys. Lett. B* **105** (1981) 219.

[48] H.B. Nielsen and M. Ninomiya, *Absence of Neutrinos on a Lattice. 2. Intuitive Topological Proof*, *Nucl. Phys. B* **193** (1981) 173.

[49] H.B. Nielsen and M. Ninomiya, *Absence of Neutrinos on a Lattice. 1. Proof by Homotopy Theory*, *Nucl. Phys. B* **185** (1981) 20.

[50] H. Neuberger, *Exactly massless quarks on the lattice*, *Phys. Lett. B* **417** (1998) 141 [hep-lat/9707022].

[51] H. Neuberger, *More about exactly massless quarks on the lattice*, *Phys. Lett. B* **427** (1998) 353 [hep-lat/9801031].

[52] H. Neuberger, *A Practical implementation of the overlap Dirac operator*, *Phys. Rev. Lett.* **81** (1998) 4060 [hep-lat/9806025].

[53] D.B. Kaplan, *A Method for simulating chiral fermions on the lattice*, *Phys. Lett. B* **288** (1992) 342 [hep-lat/9206013].

[54] R.C. Brower, H. Neff and K. Orginos, *Mobius fermions*, *Nucl. Phys. B Proc. Suppl.* **153** (2006) 191 [hep-lat/0511031].

[55] R.C. Brower, H. Neff and K. Orginos, *The Möbius domain wall fermion algorithm*, *Comput. Phys. Commun.* **220** (2017) 1 [1206.5214].

[56] T.-W. Chiu, *Optimal domain wall fermions*, *Phys. Rev. Lett.* **90** (2003) 071601 [hep-lat/0209153].

[57] V. Furman and Y. Shamir, *Axial symmetries in lattice QCD with Kaplan fermions*, *Nucl. Phys. B* **439** (1995) 54 [hep-lat/9405004].

[58] K. Naito, M. Oka, M. Takizawa and T. Umekawa, *U(A)(1) breaking effects on the light scalar meson spectrum*, *Prog. Theor. Phys.* **109** (2003) 969 [hep-ph/0305078].

[59] T. Kunihiro, *X Meson aka eta-prime and Kobayashi- Maskawa-'t Hooft Six-quark Vertex: U(1)(A) Anomaly and Generalized Nambu-Jona-Lasinio Model*, *Prog. Theor. Phys.* **122** (2009) 255 [0907.3808].

[60] J. Greensite and K. Matsuyama, *Cuprates and center vortices: A QCD confinement mechanism in a high-T_c context*, 1811.07374.

[61] C.B. Lang, *Low lying eigenmodes and meson propagator symmetries*, *Phys. Rev. D* **97** (2018) 114510 [1803.08693].

[62] M. Catillo, *On SU(2)CS-like groups and invariance of the fermionic action in QCD*, *Int. J. Mod. Phys. A* **37** (2022) 2250102 [2109.03532].

[63] P. Boyle, A. Yamaguchi, G. Cossu and A. Portelli, *Grid: A next generation data parallel C++ QCD library*, 1512.03487.

[64] S. Ueda, S. Aoki, T. Aoyama, K. Kanaya, H. Matsufuru, S. Motoki et al., *Development of an object oriented lattice QCD code 'Bridge++'*, *J. Phys. Conf. Ser.* **523** (2014) 012046.

[65] G. Cossu, J. Noaki, S. Hashimoto, T. Kaneko, H. Fukaya, P.A. Boyle et al., *JLQCD IroIro++ lattice code on BG/Q*, in *31st International Symposium on Lattice Field Theory*, 11, 2013 [1311.0084].

[66] T. Amagasa et al., *Sharing lattice QCD data over a widely distributed file system*, *J. Phys. Conf. Ser.* **664** (2015) 042058.

[67] R. Sommer, *Scale setting in lattice QCD*, *PoS* **LATTICE2013** (2014) 015 [1401.3270].

[68] C. Morningstar and M.J. Peardon, *Analytic smearing of SU(3) link variables in lattice QCD*, *Phys. Rev. D* **69** (2004) 054501 [hep-lat/0311018].

[69] D. Laudicina, M. Dalla Brida, L. Giusti, T. Harris and M. Pepe, *QCD mesonic screening masses and restoration of chiral symmetry at high T*, *PoS* **LATTICE2022** (2023) 182 [2212.02167].

[70] L. Giusti, T. Harris, D. Laudicina, M. Pepe and P. Rescigno, *Baryonic screening masses in QCD at high temperature*, *Phys. Lett. B* **855** (2024) 138799 [2405.04182].